NTNU – Trondheim
Norwegian University of
Science and Technology

Non-Linear Finite Element Analyses of Reinforced Concrete with Large Scale Elements

Including a Case Study of a Structural Wall

Jonas Stene Pettersen

Civil and Environmental Engineering
Submission date: June 2014
Supervisor: Max Hendriks, KT
Co-supervisor: Morten Engen, KT

Norwegian University of Science and Technology
Department of Structural Engineering

Summary

The accuracy of large scale elements in nonlinear finite element analyses (NLFEA) of reinforced concrete is investigated. A much used finite element analysis design procedure, used to design large offshore concrete structures, is presented, and suggestions for the utilization of NLFEA in the process is given. Means to obtain effective use of NLFEA are discussed and the importance of large elements to minimize the computational cost is stressed. The use of large elements is investigated in a case study of a structural wall. The wall is analyzed using medium scale elements that should be able to predict the behavior well, and by use of large elements. Both analysis results are compared with experimental results. The finite element models are created as they would in a design situation and the analyses are conducted without tweaking of the material parameters. State-of-the-art material models, that accurately describe the most important material characteristics of reinforced concrete, are selected. A short presentation of the smeared crack approach for finite element modeling of concrete is given. Both a fixed and a rotating crack model is used.

The results of the analyses reveal a poorly predicted ultimate load carrying capacity of the structural wall, and it is found that the missing inclusion of the volumetric expansion effect of concrete is the main cause. No significant difference is found between the fixed and the rotating crack models, a finding that is attributed to the fact that no rotation of the stress field in the structural wall is seen before the peak load. A higher load capacity is found when using large scale elements. It is believed that the higher capacity is caused by the inability of the large elements to pick up the most extreme compressive stresses in the compressive zone. Thus, the failure of the compressive zone is delayed and a higher load capacity is found. In the first phase of the deformational response the predicted behavior of the wall in the large scale analyses is found to be stiffer, due to non-localized cracks, as compared to the medium scale analyses where a localized crack pattern is observed. When the crack pattern is progressed, the difference is negligible. It is found that the all-over prediction of the wall behavior in the large scale analyses is good. The stiffness for high load levels is very accurate and the failure mode is correct. If part of a larger structure, the predicted behavior of the wall would probably allow for finding of the correct distribution of forces in the structure and the cause and progression of failure. Thus, the use of large elements in NLFEA of large structures is found to be promising. However, a lot of work remains to be done before such use can be done confidently. Suggestions for further work are given.

Sammendrag

Nøyaktigheten av store elementer i ikke-lineære elementanalyser (NLFEA) av armert betong er undersøkt. En mye brukt elementmetodebasert prosjekteringsstrategi, brukt ved prosjektering av store offshore konstruksjoner i betong, er presentert og forslag til bruk av NLFEA i en slik prosess blir gitt. Virkemidler for å oppnå effektiv bruk av NLFEA blir diskutert og viktigheten av bruken av store elementer for å begrense regnetiden blir poengtert. Bruken av store elementer er undersøkt gjennom et studie av en konstruksjonsvegg. Veggen blir analysert ved bruk av mellomstore elementer som skal være i stand til å forutse veggens oppførsel med tilstrekkelig nøyaktighet, og ved bruk av store elementer. Resultater fra begge analyser blir sammenlignet med forsøksresultater. Elementmodellene blir bygget opp slik man ville ha gjort det i en prosjekteringsprosess og analysene er gjennomført uten justering av materialparametere. Topp moderne materialmodeller blir valgt som på en nøyaktig måte beskriver de viktigste egenskapene til armert betong. En presentasjon av *smeared crack*-modellen blir gitt. Både en *fixed crack*- og en *rotating crack*-modell er brukt.

Analyseresultatene viser at veggens lastkapasitet blir dårlig estimert og det konkluderes med at det mest sannsynlig skyldes at den volumetriske ekspansjonen av betongen ikke er representert i materialmodellene som er brukt. Ingen signifikante forskjeller mellom *fixed crack*- og *rotating crack*-modellene blir funnet, noe som tilskrives det faktum at ingen rotasjon av spenningsfeltet i veggen finner sted før lasttoppen. En høyere kapasitet predikeres når det benyttes store elementer, noe som trolig skyldes at integrasjonspunktene i de store elementene ikke klarer å fange opp de mest ekstreme spenningene i trykksonen. Altså forsinkes sammenbruddet av trykksonen og en høyere lastkapasitet predikeres. I den første fasen av veggens deformasjon viser storskala-analysene en stivere oppførsel enn mediumskala-analysene, trolig grunnet fraværet av et lokalisert rissmønster i førstnevnte analyser. Når rissmønsteret utvikles videre er forskjellen i stivhet neglisjerbar. Veggens oppførsel predikeres med god nøyaktighet i storskala-analysene. Nøyaktigheten av stivheten ved høy belastning er meget god og bruddformen som predikeres er korrekt. Dersom veggen var en del av en større konstruksjon ville det mest sannsynlig være mulig å finne den korrekte fordelingen av krefter i konstruksjonen, samt årsaken til, og utviklingen av brudd. Altså er det funnet at bruken av storskala-elementer i NLFEA av store konstruksjoner er lovende. Det påpekes likevel at mye arbeid gjenstår før sikker bruk kan gjøres. Forslag til videre arbeid er gitt.

Preface

This master's thesis was written during the spring semester 2014 and concludes my 5 year education at the Norwegian University of Science and Technology (NTNU). The thesis was written at the Department of Structural Engineering (KT) at the Faculty of Engineering Science and Technology.

The thesis is a part of an ongoing work by PhD candidate Morten Engen. The aim of his work is to develop procedures for utilizing nonlinear finite element analysis in the design of large concrete structures. A part of this work seeks to map the effects of element size on the analysis result, and hopefully find out how large scale elements can be used in nonlinear finite element analyses while still securing sufficient accuracy. Hopefully, this thesis will supply some valuable input on this subject. A substantial amount of time has been invested in the research of theory related to the material behavior and numerical modeling of reinforced concrete, both fields of which I was only partly familiar with before the work on this thesis was started. All analyses in this thesis were conducted using the DIANA finite element software package, version 9.4.4. Learning to use the program and working around its shortcomings has been time-consuming. But, in the end the program has produced highly sophisticated analysis results.

I want to thank my supervisor Prof.dr.ir. Max A.N. Hendriks for valuable help and guidance. I also want to thank my co-supervisor M.Sc. Structural Engineering, Research Fellow at Multiconsult, Morten Engen. Through hours of discussions he has provided me with excellent guidance and motivation, and increased both my knowledge and interest for finite element analysis of concrete structures. Finally, I would like to thank my fellow student, and good friend, Johan H. Martens, for proofreading my thesis.

Jonas Stene Pettersen
Trondheim, June 2014

Contents

List of Figures

List of Tables

1 Introduction

Finite element analysis (FEA) has been applied to problems in the field of concrete structures for over 50 years. The method has given analysts the tools necessary to solve complex problems and has been vital in the design process of many structures built in the second half of the 20th century. Especially in the design of offshore structures, FEA has been widely used with great success. However, this is also an area of application where the pitfalls of the method have become apparent. Often referred to is the collapse of the Sleipner A platform in 1991 where a combination of poor finite element modeling and deficient shear reinforcement caused the collapse of a two billion NOK structure [1, 2, 3]. Analyses performed during the design of large concrete structures have traditionally utilized a simplification of the global structural response by using linear analysis to find the load distribution in the structure, a simplification that makes it possible to monitor the analyses in a practical way and also drastically reduces the computational cost. However, this is a simplification that must be done with care as it disrespects the concrete as a brittle fracture material and consequently, it will not yield the correct structural repsonse.

> "*The one type of nonlinearity that is expected in all concrete structures is cracking. This phenomenon is difficult to account for in a simple fashion, yet is vital in making realistic estimates of structural stiffness*"
>
> - fib Bulletin 45 [4].

In order to find the correct structural response, nonlinear finite element analysis (NLFEA) must be utilized. The step from linear finite element analysis (LFEA) to NLFEA introduces many additional challenges and the solving of the equation system is no longer straight forward. The interaction between the brittle and inhomogeneous concrete material and the ductile reinforcement steel is complicated and difficult to describe mathematically, and examples from the literature have shown that even the simplest structures can present the analyst to great challenges [1]. In order to capture the local effects of cracking, and predict the structural behavior on a global level with sufficient accuracy, the NLFEA should comprise among other parts suitable material models, finite elements that can describe the relevant deformations, and a stable and accurate solution procedure. Generally, smaller elements are more accurate than larger elements and in linear finite element analyses the use of large elements may yield considerable challenges when it comes to describing the structural behavior. When, in addition,

the nonlinear behavior of concrete is respected the use of large elements is even more challenging. As of today, it is not effective nor manageable to perform NLFEA of large structures if the finite element size is small. Thus, if NLFEA is to be utilized in the design process of such structures the finite element model must yield satisfactory results even for rather large element sizes.

This thesis aims to investigate the transition from medium to large scaled elements through a case study of a well documented experimental work. The effects of the transition will be discussed with respect to the structural behavior, the prediction of the ultimate load capacity, and the crack pattern observed in the structure. In the end, this investigation should yield some valuable insight into the behavior of reinforced concrete structures analyzed with large scale elements, and be of help to further work aiming to utilize the power of NLFEA in the design process of larger structures.

A brief review of the forthcoming chapters: Chapter 2 discusses the material behavior of concrete both qualitatively and mathematically. Chapter 3 presents a state-of-the-art FEA design procedure and suggestions for the utilization of NLFEA in such a procedure is given. Chapter 4 presents the case study performed. First of all, experimental results obtained by Lefas et al. is reported. Secondly, the different element scales are presented based on a theoretical approach and element sizes used for the NLFEAs conducted are selected, based on preliminary analyses. Thirdly, the finite element models are presented and relevant material parameters are calculated. At last, the key results of the NLFEAs are presented. In chapter 5 the results of the analyses are discussed and the effects of the element size on the analysis result is presented. Chapter 6 contains the concluding remarks and chapter 7 presents suggestions for further work. Two appendices are enclosed. The first contains a presentation of the different finite element generations used. The second contains a presentation of the problems encountered in the finite element program used, and the solutions found.

2 Materials

In this chapter the characteristics of concrete and reinforcement steel are described qualitatively, and mathematical material models capable of reproducing the behavior of the two materials are selected.

2.1 Qualitative Description

The material behaviour of concrete differs from the behavior of other videly used materials like steel or aluminum. Where steel and aluminum are generally assumed to behave as homogenous isotropic materials, with equal mechanical properties in both compression and tension, the material behaviour of conrete is more complex. The material response is largely affected by it's non-homogenous nature: the composition of aggregate and mortar. Due to this composition, microcracks are present in the material before any loading is applied and interaction between the aggregate and the mortar during loading causes new cracks to appear and existing cracks to propagate. In concrete under monotonic loading, the effects of this crack propagation are easily observed. For low load levels the microcracking does not affect the material at large and it exhibits an almost isotropic behavior. At some point the appearance of macrocracks abolishes the isotropy and the behavior beyond this point is anisotropic, governed by the crack directions.

2.1.1 Compression Response

The compression response of concrete can be described by considering a uniaxially loaded cylinder. The response from a uniaxial cylinder test, shown in figure 2.1, is almost linear until the stress reaches about 30% of the ultimate strength [5]. At this point, existing microcracks between the aggregate and the mortar increase in size and new cracks arise, causing the stress-strain curve to deviate from the linear response. When the stress is approaching the ultimate strength these cracks start to connect and continuous crack patterns through the mortar between individual pieces of aggregate are formed. When such continuous crack patterns develop in large areas of the specimen the ultimate strength is reached. Usually, concrete in compression is assumed to exhibit a softening effect for post-peak loading but this behavior is disputed. Some researchers consider the softening effect essential in proper modeling of concrete. Others indicate that this effect is merely a consequence of interaction between the concrete specimen and the machine used to test it, and that a sudden loss of load-carrying capacity when the compression strength is reached is more correct [6].

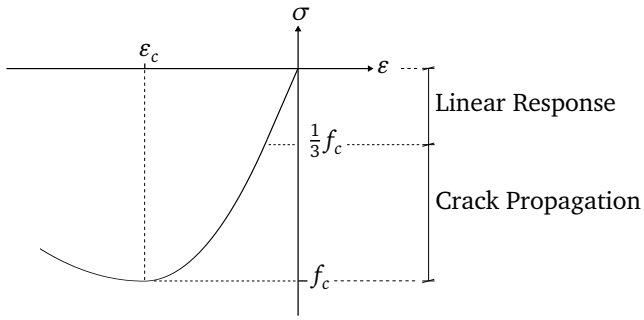

Figure 2.1: *Compression response of concrete*

2.1.2 Lateral Stresses

The compressive behavior of concrete is greatly affected by lateral stresses. Kupfer et al. [5] investigated this behavior in 1969 by conducting a series of tests on biaxially loaded concrete cubes. The results shown in figure 2.2 clearly showed an increase in strength when lateral confinement stresses were present and a decrease in strength for lateral tension stresses. The increase in strength is due to the inhibition of microcrack propagation in the material caused by the lateral confinement stresses. The delayed propagation of the cracking process also causes the concrete to exhibit a more ductile behavior [2]. A more recent report by Vecchio and Collins [7] further investigated the compressive nature of concrete with respect to lateral cracks. Existing experimental data was reviewed and a significant reduction of the compressive strength for laterally cracked concrete was observed. Lateral cracking also influenced the ductility of the concrete, as results showed a reduced strain at peak stress when lateral cracks were present.

2.1.3 Volumetric Expansion

An important feature of concrete subjected to compression is the course of the volumetric strain. Figure 2.3 shows the volumetric strain of concrete subjected to uniaxial compression. Positive values of volumetric strain represent volumetric reduction. As is expected the volume decreases as the compression stress is increased. However, when about 80-95% of the compression strength is reached the volume starts to increase, i.e. the minimum volume is reached [2, 5], as a consequence of the formation of continuous crack patterns in the concrete as described in section 2.1.1. Further loading will eventually cause an increase beyond the initial unloaded volume. This volumetric expansion may cause cracking in highly stressed compressive zones in concrete due

to an effect termed ”splitting”. Splitting occurs when a highly stressed concrete area expands and lesser stressed neighboring areas are forced to expand as well, the result is lateral cracking in those neighboring areas.

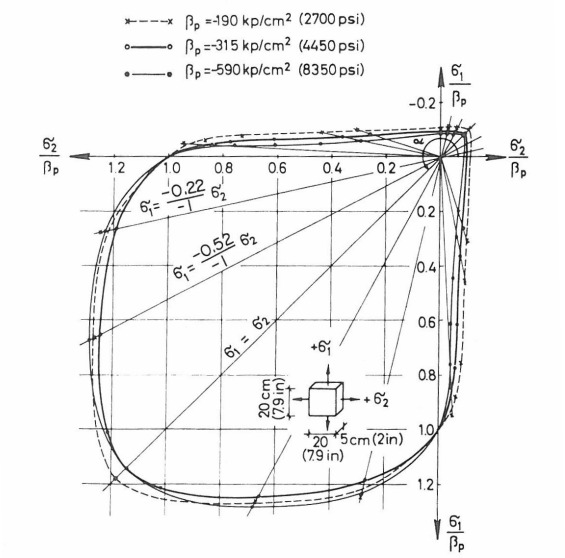

Figure 2.2: *Biaxial strength of concrete from experimental results*
β_p = *unconfined uniaxial strength [5]*

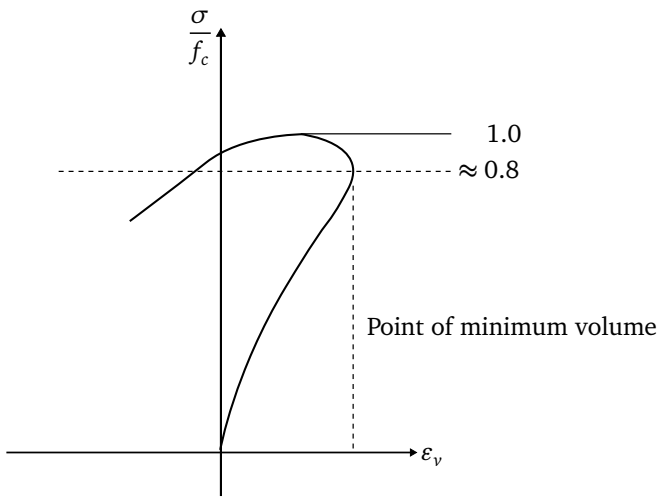

Figure 2.3: *Volumetric strain of concrete subjected to uniaxial compression*

2.1.4 Tension Response

As opposed to steel and aluminum, where the compressive strength and the tensile strength is generally assumed to be equal, the tensile strength of concrete is usually only about 5-10% of the compressive strength. An almost linear relation between stresses and strains is observed for a uniaxially loaded cylinder in tension, until the tensile strength is reached and cracking occurs. Post-peak loading shows a tension softening effect which is caused by crack growth in the cylinder. To observe this post-peak behavior, displacement control must be applied to the experiment or loading must be applied in parallel to other specimens that are stiffer than the steepest negative tangential stiffness of the post-peak curve [8]. If load control is applied without special care, the experiment will yield a brittle fracture as soon as the tensile strength is reached. The background documentation of *fib* Model Code 2010 [9], states that tension softening can have a large influence on the tensile capacity of a tested member. However, it is pointed out that the influence of this effect is very small, if not negligible, in large scale members with sufficient reinforcement in bending and shear. Thus, the tension softening effect is not that important in analyses of structures designed using a design code.

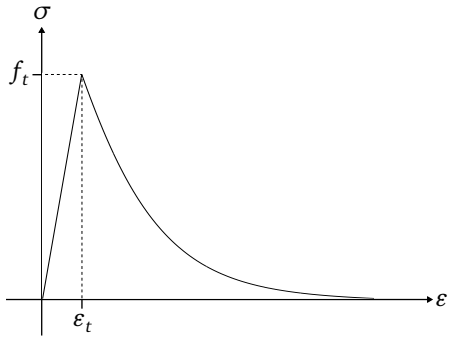

Figure 2.4: *Tension response of concrete*

2.1.5 Reinforcement

Reinforcement steel is normally described as a ductile isotropic material with an elastic-plastic material behavior, and plastic hardening. The material behavior of the reinforcement steel itself is not problematic to reproduce in finite element analyses of reinforced concrete, and will not be further discussed.

2.1.6 Interaction Between Concrete and Reinforcement

Figure 2.5 shows how cracking spreads out along a reinforcement bar embedded in concrete [4]. There are bond cracks that occur when the reinforcement and the concrete are displaced relative to each other, a phenomenon called bond slip, and there are major concrete cracks that extend to the surface of the concrete. An important effect to take into account in finite element modeling of concrete, is the added stiffness that the concrete in between the fully developed cracks represents, as compared to a bare steel bar [4]. The added stiffness is caused by the tensile capacity of concrete before and during opening of a crack. This contributes to the stiffness of a reinforced concrete bar as the one in figure 2.5. However, yielding of the reinforcement will always initiate at the point of a fully developed concrete crack, where the concrete tensile stresses are zero. Thus the concrete will not help increase the capacity of the reinforced concrete bar, only the stiffness before yielding of the reinforcement. On a material level, the concrete tensile stresses transferred after initiation of each crack is called tension softening. On a structural level, the combined stiffness contribution of all cracks is called tension stiffening.

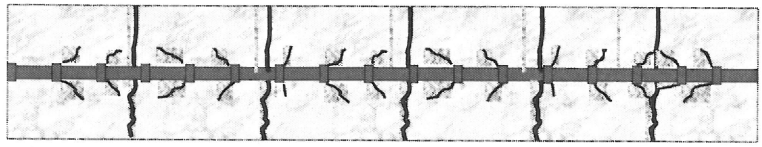

Figure 2.5: *Cracking along a reinforcement bar [4]*

2.2 Mathematical Modeling

As described in section 2.1, concrete is a non-homogenous material consisting of aggregate and mortar and its behavior is perhaps most correctly reproduced by modeling this composition. However, modeling the aggregate and mortar and the interaction between them explicitly is not practical in general modeling. Most material models available therefore consider concrete as a homogenous material, and the behavior is described by parameters calibrated from tests performed on larger specimens. Usually the result of a uniaxial cylinder test is sufficient. The material models used for both concrete and reinforcement steel were selected according to guidelines issued from Rijkswaterstaat (part of the Dutch Ministry of Infrastructure and the Environment) in May 2012 [10], from now on referred to as the Dutch Guidelines. The guidelines were issued to help analysts perform robust NLFEA and consist of state-of-the-art procedures that are considered to be ”best practices for nonlinear finite element simulations of concrete” [10]. Combined, the material models selected should be capable of reproducing the behavior of reinforced concrete with satisfactory accuracy, and the most important material characteristics are respected.

2.2.1 Smeared Cracking

Two main approaches for model the cracking of concrete are found in the literature: the discrete crack model and the smeared crack model. One of the first attempts at modeling the cracking of reinforced concrete featured a discrete crack model, where cracks were represented by disconnecting nodes between elements when the strain implicated that cracking was present [2]. The node-splitting is illustrated for a simple mesh in figure 2.6(b). A more sophisticated version of the discrete crack model may contain an algorithm that continuously re-meshes the model in favor of the crack directions as the cracking progresses. The discrete crack approach is computationally expensive as the node-splitting and re-meshing require a reassembly of the stiffness matrix when a new crack is formed. Thus, the discrete crack model is not suitable, and almost never used, for general analysis of reinforced concrete structures. However, for research purposes where the crack pattern is known in advance, the method may be very useful. For most analysis purposes, the smeared crack model is the preferred method of choice. In this model, as opposed to modeling cracks explicitly, the effect of several cracks is smeared over the volume represented by each integration point in the element mesh, as illustrated in figure 2.6(c). One of the great advantages of the smeared crack model is that the formation of cracks is much more independent of the element mesh and the position of the nodes, compared to the discrete crack model [11].

There is no need for a change in the element mesh after crack formation, or for the analyst to place nodes in certain positions where cracking is believed to occur. Cracks will form in the area represented by the integration points where the stress state is most critical. This approach avoids the computationally costly re-meshing associated with the discrete crack model.

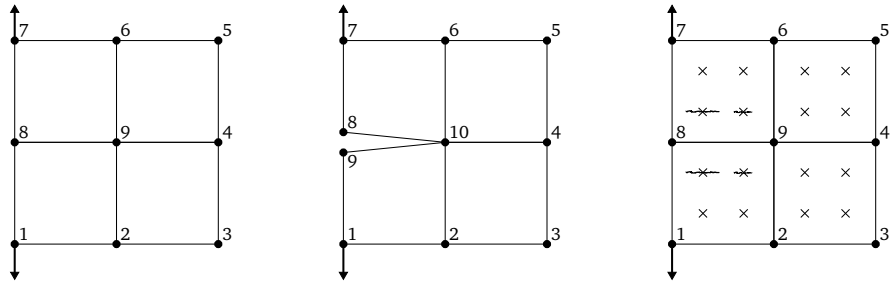

(a) *Uncracked* **(b)** *Discrete cracking* **(c)** *Smeared cracking*

Figure 2.6: *A simple mesh modeled with discrete and smeared cracking*

For the analyses performed in this thesis the Total Strain smeared crack model was used. The model is based on the Modified Compression-Field Theory developed by Vecchio and Collins 1986 [12], and assumes that cracks are formed perpendicular to the direction of the principal tensile strain. The principal stress axes and the principal strain axes are assumed to coincide. Upon formation of a crack, the material is modeled as isotropic and the stresses and strains are evaluated in the principal directions. After the formation of a crack, the material is considered orthotropic with material axes aligned according to the condition at crack initiation [13]. The stiffness upon crack formation is evaluated in the direction of the crack. Two different formulations of the Total Strain smeared crack model was used. The first is the fixed crack model where the direction of a crack is fixed when the crack is formed. In post-crack loading the stresses and strains at the point of the crack are evaluated in the direction of the initial crack, all though the directions of the principal strains might actually have rotated. A second crack is allowed to form if the tensile stress in the direction orthogonal to the normal of the first crack exceeds the tensile strength of the concrete.

The second formulation of the Total Strain smeared crack model used was the rotating crack model. Stresses and strains after crack formation are here evaluated in the principal strain directions, and a rotation of the principal axes is therefore taken into account. A second crack will form as soon as the principal tensile stress exceeds

the tensile strength, regardless of the direction of the stresses.

A simplified version of the cracked material stiffness matrix that is used in the smeared crack concept is displayed in equation (2.1) [13]. The subscripts in the matrix refer to the n,s,t-axis directions of the crack where n refers to the direction normal to the crack and s,t refer to the directions tangential to the crack. The mathematical background of the theory will not be presented here. However, some important characteristics of the stiffness matrix will be discussed.

$$\begin{bmatrix} \sigma_{nn} \\ \sigma_{ss} \\ \sigma_{tt} \\ \sigma_{ns} \\ \sigma_{st} \\ \sigma_{tn} \end{bmatrix} = \begin{bmatrix} E_{nn} & E_{ns} & E_{nt} & 0 & 0 & 0 \\ E_{ns} & E_{ss} & E_{st} & 0 & 0 & 0 \\ E_{nt} & E_{st} & E_{tt} & 0 & 0 & 0 \\ 0 & 0 & 0 & G_{ns} & 0 & 0 \\ 0 & 0 & 0 & 0 & G_{st} & 0 \\ 0 & 0 & 0 & 0 & 0 & G_{nt} \end{bmatrix} \begin{bmatrix} \varepsilon_{nn} \\ \varepsilon_{ss} \\ \varepsilon_{tt} \\ \gamma_{ns} \\ \gamma_{st} \\ \gamma_{tn} \end{bmatrix} \tag{2.1}$$

Early versions of the smeared crack model featured a stiffness matrix like the one in equation (2.1), where the terms E_{nn}, E_{ns}, E_{nt}, G_{ns} and G_{nt} where set equal to zero [13]. In other words, the stiffness in the direction normal to the crack was lost completely once the crack occurred. The expansion effect due to Poissons' ratio and the shear stiffness in the tangential directions were also abolished. This simplification is arguably not correct, as some researchers claim that concrete is capable of transmitting tensile forces even in a cracked phase, and shear forces through a crack due to aggregate interlock [13]. Other researches claim that aggregate interlock in concrete represents almost no significant resistance against shear forces. Kotsovos et al. argument that such shear resistance can only be activated by a shear movement of the crack faces and that such movement contradicts the cracking process of concrete, where cracks open in the direction of the maximum tensile (or the minimum compressive) principal stress [14]. Regardless of the disputed physical significance of aggregate interlock, it is advisable to transfer a certain shear stiffness across cracks to avoid numerical trouble, due to an abrupt discontinuity [15]. This is also true for the normal crack stiffness, at least when a significant amount of cracking occurs at the same time. It is not necessary to adjust the post-crack shear stiffness if the rotating crack model is used since this model always evaluates the stresses and strains in the principal directions. The degradation of the shear stiffness in the fixed crack model is handled by a shear retention factor β, with a value between 1 and 0, that is multiplied with the pre-cracking shear moduli G_{ns} and

G_{nt} upon cracking. The shear retention factor is further discussed in section 2.2.5.

None of the smeared crack approaches presented in this section are correct representations of the cracking process. The fixed crack model is perhaps the most physically correct one given that once a crack has occurred it is not allowed to change direction. However, in an experiment subsequent cracks in an area could be found to form in directions different from the first crack observed. Then the initial direction in which a crack is formed may not be representative for all cracks in the area covered by an integration point in a finite element model, at least for large elements. Thus, the fixed crack model may appear to stiff if the stress field rotates significantly after the first crack appears, but not so much that the second orthogonal crack will form. The rotating crack model on the other hand allows for this rotation to occur. However, rotation of an existing crack is a somewhat unphysical phenomenon.

One key aspect of the smeared crack approach is that the smeared cracking process should be energy-equivalent to the actual cracking process. A convenient way of obtaining this equivalency is by controlling the cracking process by a crack bandwidth and a measure of the fracture energy [11]. The fracture energy is given as the energy released during the formation and opening of a crack per unit area of the crack surface, i.e. the out-of-plane surface of the cracks shown in figure 2.7. The crack bandwidth is the in-plane width of the area that contributes to the fracture process, denoted h in the figure. The cracking process of reinforced concrete not only consists of visible macrocracks as shown in figure 2.7, there are also smaller non-visible microcracks. All these cracks contribute to the energy release of the fracture process, and the crack bandwidth must therefore cover the total width over which they occur. The fracture energy divided by the crack bandwidth equals the total energy released from the volume represented by a crack. In an element mesh, the fracture process of an integration point is distributed over a crack bandwidth which is determined according to the element size. When the energy of the crack is released over the same width, dependency of the mesh size is minimized [11]. If the calculated crack bandwidth surpasses the physical crack bandwidth of the concrete, due to a large element size, measures must be taken to again achieve the energy-equivalency of the fracture process. The crack bandwidth must then be limited to the crack bandwidth expected to occur in the concrete, i.e. the width extending from a macrocrack and half-way to the next macrocrack in either direction, as illustrated in figure 2.7. The crack bandwidth is thus limited by the crack spacing, which can be calculated. The fracture energy based approach can be used for both tensile cracking and compressive crushing of concrete.

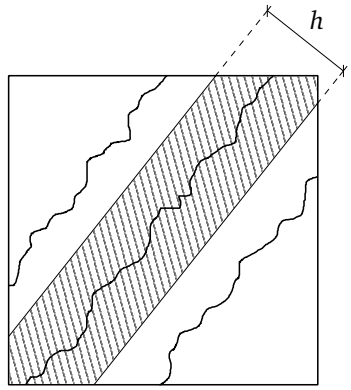

Figure 2.7: *Crack bandwidth*

2.2.2 Compression Response

The compression response was modeled by a parabolic curve formulated by Feenstra 1993 [16], as shown in figure 2.8. The stress-strain relation is linear until the stress reaches $1/3$ of the compression strength, after which the slope of the curve decreases. When the compression strength is reached, and cracking occurs, the stress is gradually decreased until the ultimate strain is reached. The value of the ultimate strain is chosen such that the area under the curve is equal to the fracture energy in compression G_c $[{}^{Nmm}/_{mm^2}]$, divided by the crack bandwidth, i.e. the amount of energy dissipated during the crushing process. When determining the ultimate strain in this way the element size dependency is minimized and the fracture process is in agreement with the energy-equivalency described in section 2.2.1. It should be commented that the softening branch for post-peak loading may not be a physical material behavior as pointed out in section 2.1.1. According to the background documentation of *fib* Model Code 2010 [9], the descending branch of the stress-strain diagram of concrete in compression is not of importance when investigation the structural deformations under ultimate load. The appearance of a descending branch is dependent on the load redistribution possibilities of the specimen tested and, if present, the descending branch is strongly dependent of the type of specimen and it's boundary conditions. However, the softening branch is present in the Modified Compression-Field Theory and was therefore used for the analyses carried out here, regardless of its disputed importance.

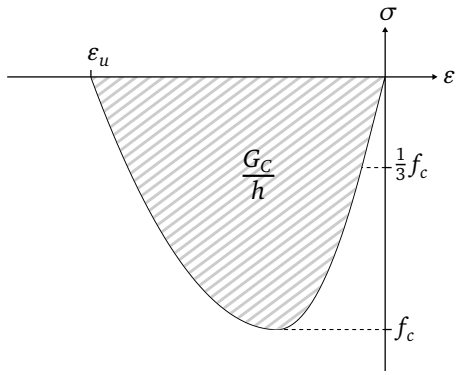

Figure 2.8: *Parabolic compression [17]*

2.2.3 Lateral Confinement and Lateral Cracking

To account for the large changes in strength when biaxial or triaxial stress states are present, a lateral confinement model and a lateral cracking model were chosen. The lateral confinement model uses a failure surface defined by Hsieh-Ting-Chen [17] and the strength parameters K_σ and K_ε, applied to increase the compressive strength and corresponding strain, are determined from a formula by Selby and Vecchio [2]. The increased ductility under multiaxial compressive stress (cf. section 2.1.2), is accounted for by modifying the descending branch of the stress-strain curve. The effect of both the stress and strain increase, and the ductility modification is shown in figure 2.9(a). The lateral cracking model used, is Model B by Vecchio and Collins [7]. The compressive strength is reduced according to the the lateral cracking present by a factor β_{cr}, as shown in figure 2.9(b). The strain is not modified. It should be mentioned that the model by Vecchio and Collins does not reduce the compressive strength before the lateral stresses exceed the tensile strength, i.e. no reduction takes place before lateral cracks are present. The model therefore omits the linear reduction shown in figure 2.2.

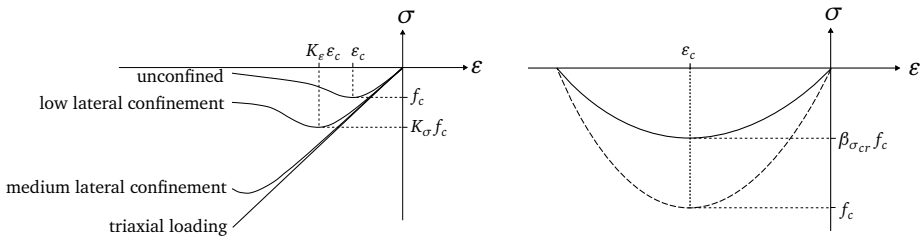

(a) *Lateral confinement* **(b)** *Lateral reduction*

Figure 2.9: *Stress-strain curve in compression*

2.2.4 Poisson Effects

The finite element program used for the analyses in this thesis does not offer the possibility to model the volumetric expansion discussed in section 2.1.3, the Poisson's ratio is kept constant regardless of the volumetric stress state. However, the ratio is reduced when cracking occurs, as discussed in section 2.2.1. A reduction of the ratio is believed to produce more realistic results in NLFEA of reinforced concrete [18]. When in a cracked state, Poisson's ratio is gradually reduced to zero between the direction normal to the crack and the direction(s) parallell to the crack. The stiffness terms E_{ns} and E_{nt} in equation (2.1) [13] are reduced accordingly.

2.2.5 Shear Retention Factor

For the fixed crack model, a shear retention factor β was used to retain some shear resistance in cracked integration points. The factor can be specified in two ways, either a constant shear retention factor is used and the parameter is fixed at a value between 1 and 0, or a variable shear retention factor is used where the parameter is set to 1 immediately upon cracking and gradually reduced to 0 according to the secant stiffness of the tension response in post-cracking. Severe convergence problems were encountered when using a variable shear retention factor. Thus, a constant shear factor of 0.1 was specified for the fixed crack model. This value was chosen based on the argumentation by González et al. that such a low value is in agreement with the claim that significant shear stresses are not present in concrete cracks [15]. This value is also sufficiently high as to avoid numerical problems.

2.2.6 Tension Response

The tension response is modeled as linear until the tensile strength is reached. An exponential softening curve was used to model the tension softening effect, as shown in figure 2.10. The shape of the curve is defined by the the maximum tensile strength f_t, and the ultimate strain ε_u, calculated according to equation (2.2). The ultimate strain is determined such that the area under the curve equals the amount of energy dissipated during the forming and opening of a crack. By determining the area of the curve in this way the energy of a crack is released over the same width as it is distributed over and the energy-equivalency of the fracture process is secured. As for the crushing process, this energy based approach helps minimize the element size dependency.

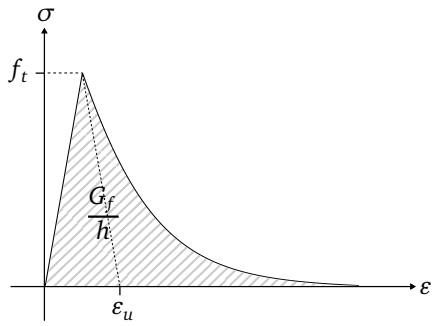

$$\varepsilon_u = \frac{G_F}{h f_t} \qquad (2.2)$$

Figure 2.10: *Exponential softening*

2.2.7 Reinforcement

The reinforcement was modeled as elastic-plastic with linear strain hardening. A trilinear stress-strain relationship was used to avoid numerical trouble, due to an abrupt change in stiffness when the stress exceeds the yield strength in a load step. The stress-strain relationship is defined by the initial Youngs modulus, a modified modulus calculated according to Kotsovos et al. 2008 [19] when the stress approaches the yield strength, and the ultimate strain calculated according to the Dutch Guidelines [10]. The trilinear stress-strain curve is illustrated in figure 2.11. Due to unexpected convergence problems, a bilinear stress-strain relationship was used in the large scale analyses. The problems encountered with the trilinear curve are discussed in appendix B.3. Bond slip was specified according to *fib* Model Code 2010, as illustrated in figure 2.12. The model consists of a bond curve that specifies the relationship of the slip between a reinforcement bar and the confining concrete, and the traction stress that is transferred between them. Good bond conditions were assumed, $\tau_{bmax} = 2.5\sqrt{f_{cm}}$ and the values

for s_1, s_2 and s_3 were set to 1, 2 and 20 mm, respectively. Note that bond slip was only accounted for in the medium scale analyses, as will be discussed further in section 4.2.1.

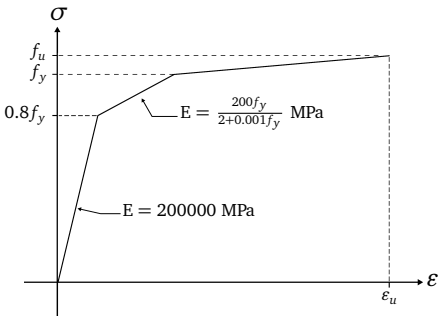

Figure 2.11: *Trilinear stress-strain curve of reinforcement steel*

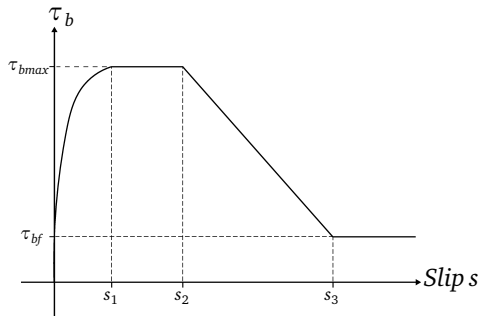

Figure 2.12: *Bond slip model from fib Model Code 2010 [20]*

2.2.8 Tension Stiffening

The tension stiffening effect discussed in section 2.1.6 was taken into account by use of a tension softening model for the concrete and a bond slip relation for the interaction between the concrete and the reinforcement. This approach will properly model the tension stiffening effect while stress contribution from the concrete at yield of the reinforcement is avoided [4]. For an element size small enough to capture variations in the stress field, the approach to tension stiffening used should yield a degree of localization in the crack pattern. When large elements are present, a localized crack pattern should not be expected. Also, the use of a bond slip model is no longer justifiable with large scale elements, as will be discussed further in section 4.2.1, and perfect bond was therefore assumed. The tension stiffening effect in the large scale analyses was modeled by means of a tension softening model for the concrete alone. To attain the correct magnitude of the stiffness contribution of the tension stiffening effect, the fracture energy was adjusted according to the crack spacing of the structure, as is further discussed in sections 4.2.1 and 4.4.2. Concrete stress contribution at yielding of the reinforcement was avoided because the ultimate tensile strain in the concrete is lower than the yield strain of the reinforcement.

3 Applications for Design

To put the scope of this thesis into a larger context, this chapter discusses how NLFEA can be used in the design process of large concrete structures. The use of LFEA in the design process of large structures is widespread. The method offers the possibility to perform limit state design on structures of all forms. Linear analyses also allow for the use of the principle of superposition, so that a large number of load combinations may be handled effectively while still limiting the computational time to an acceptable level. In this chapter, a brief review of a state-of-the-art LFEA design procedure is given and a suggestion for the use of NLFEA in combination with this procedure is presented . Advantages, disadvantages and limitations of both LFEA and NLFEA are identified.

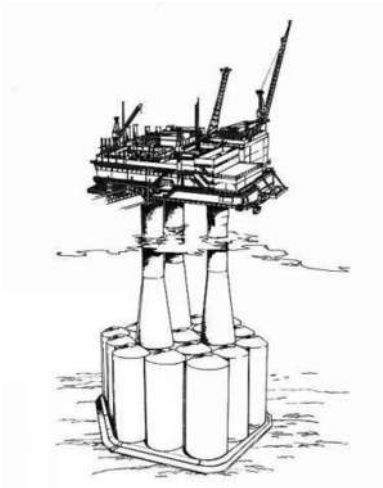

Figure 3.1: *Typical offshore concrete structure*

3.1 The Use of FEA in the Design Process

The FEA design process presented is described by Brekke et al. [21]. Is used by Multiconsult AS in the design of large offshore structures, like the one illustrated in figure 3.1, destined for operation in the north sea. The design process is divided into three main stages, as illustrated in figure 3.2: Global linear finite element analysis of the structure, post-processing of the analysis results and non-linear sectional design.

3.1.1 Design Stages

The first stage of the design process starts with an initial modeling of the structure at hand. Prior to this modeling, the key geometric aspects of the structure are determined by taking into account the presumed critical load actions. Global LFEAs are performed individually for all relevant load cases, and each analysis will result in an internal distribution of the forces acting on the structure in the given load case. In the next stage, design sections are chosen on basis of the finite element mesh and a post-processor transforms the stresses in the elements to sectional forces (normal- and shear forces and moments). The sectional forces of various load cases are then combined by linear superposition to generate load combinations for each section of the structure. In the final stage, all sections are designed on the basis of the sectional forces in the most critical load combination found in the previous stage. Non-linear material behavior of concrete and reinforcement is taken into account. In an iterative process, the positions, cross sectional areas and number of reinforcement bars are adjusted until the section is able to withstand the outer forces.

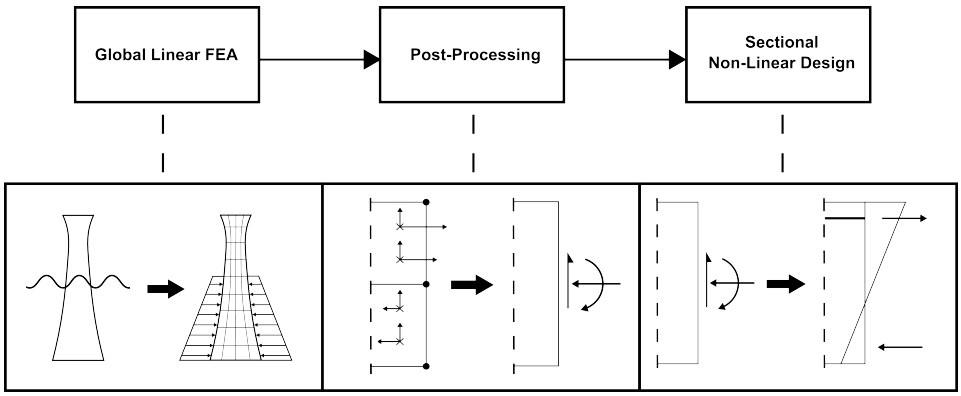

Figure 3.2: *Illustration of the FEA design process*

3.1.2 Advantages and Disadvantages

The obvious advantage of this design approach is the use of linear superposition to handle load combinations in an effective manner. When there are hundreds of load cases, it is simply not possible to perform global FEA for all the relevant load combinations, the computational cost would be immense. When load combinations are handled on a sectional level, the approach is both effective and possible to monitor in an organized way. One of the shortcomings of the process is the use of LFEAs for finding the inter-

nal load distribution of the structure, in combination with non-linear sectional design. Cracking of concrete and yielding of reinforcement can lead to significant redistribution of internal forces as the structure approaches the ultimate limit load and this effect is not reproduced when the linear material behavior is used in the global LFEAs. Thus, the global load distribution found is not correct. In the sectional design, the redistribution of forces between concrete and reinforcement during deformation within each section is correctly accounted for, but there is no strain compatibility between the various sections of the structure and hence, redistribution on a global level is not accounted for. However, it is generally assumed that as long as equilibrium between internal and external forces is found, the material strengths are not exceeded, and sufficient ductility of each section is secured, the approach yields a conservative lower bound solution. Thus, the load distributions from the LFEAs are acceptable and redistribution of forces between sections should be possible. An implication that favors the use of LFEAs is that the reinforcement need not be known before conducting these analyses. If NLFEA is to be used for finding the internal load distribution, the reinforcement must be known in advance and thus the initial analyses become part of an iterative process until the correct reinforcement layout is found. This would be computationally costly.

3.2 Suggestions for the Use of NLFEA

From a theoretical point of view it would be desirable to run full NLFEAs for all load combinations, to check the structural capacity and load redistribution thoroughly. However, as pointed out in section 3.1.2, even performing LFEAs of all load combinations is unrealistic. Also, when doing NLFEA the load sequence is of importance and hence the number of analyses necessary to conduct, in order to check all load combinations, would be extensive. Instead of replacing the linear procedure, NLFEA should be put to use where LFEA is insufficient.

3.2.1 Use of NLFEA in the Design Process

Using NLFEA means introducing some sort of non-linearity. For the case of large reinforced concrete structures, some non-linearities, like geometric non-linearity and contact, are not relevant for the structure as a whole and are best handled by separate analysis of smaller parts of the structure. Such analyses are also very computationally costly. On a global structural level it seems that material non-linearity is of most relevance. Full NLFEA of the structure with non-linear material behavior will enable the analyst to find:

- The correct distribution of forces on a global level
- The correct ultimate load carrying capacity of the structure
- The cause and progression of failure

NLFEAs can be used to perform a virtual experiment on the structure for selected critical load combinations. The load combinations chosen for such analyses could be of such a nature that the sufficiency of the LFEAs are questioned. E.g. if it is believed that extensive load redistribution will be necessary. In such cases NLFEA can be a useful tool for checking the global capacity thoroughly.

3.2.2 Effectiveness

To ensure effective use of NLFEA in the design process of complex structures, the method must be robust, easy to set up and computationally cost-effective. The material models must be able to deliver accurate results regardless of the stress-state in the structure, both in 2D and 3D, and still demand as few input parameters as possible. Preferably the only input parameter needed would be the compressive strength, which is often the only known material parameter in the design phase. When conducting NLFEA of large structures, one must keep in mind that when iterating to find convergence the shear number of nodes and integration points will often demand unacceptably large amounts of computational power and time unless proper precautions are made, even if the solution converges fast. To limit the computational cost, the NLFEAs must be able to produce usable results with rather large elements. Apart from being computationally effective, a large element size would also mean that the existing global finite element model of the structure, which is normally updated along with design revisions, could be used directly for the NLFEAs. Time consuming work to create a separate FE model is thus avoided. To minimize the computational time, the solution algorithm used must be able to find convergence with a low number of load steps and few iterations within each step. The algorithm should also be rather insensitive to step size and it should be able to pass critical points, e.g. cracking and yield of the reinforcement.

4 Case Study

The aim of this thesis is to investigate the effect of element size on the results of NLFEA of reinforced concrete. A well documented experiment reported by Lefas et al. was chosen as the case study through which this effect was investigated. In this chapter, the experiment performed by Lefas et al. will be presented. The element sizes used will be determined with respect to both the material characteristics and the structural aspects. Finally, the finite element models are described in detail and the results of the analyses are presented.

4.1 Structural Walls Tested by Lefas et al. 1990

The finite element analyses performed in this thesis are based on an article by Lefas et al. 1990 [14]. In the article, a series of reinforced concrete structural walls were tested under monotonically increasing loading, and failure modes are presented and discussed. In this section, a brief summary of the test setup is given and the main results of the article are presented. Some results from the experiment are presented along with the results of the NLFEAs in section 4.5.

4.1.1 Geometry and Loading

The wall chosen for the NLFEAs in this thesis was specimen SW21, with geometry and reinforcement as shown in figure 4.1. The wall dimensions are 650 x 1300 x 65 mm (width, height and thickness). The wall was connected to a top and a bottom beam to ensure sufficient anchoring of the reinforcement, and a fixed wall base. Monotonic loading was applied horizontally through the top beam until failure. Measurements performed during loading showed no rotation of the bottom beam, and thus the intended rigid foundation of the wall was confirmed. The out-of-plane displacements of the wall were found to be negligible, and thus the specimen was said to experience only in-plane actions.

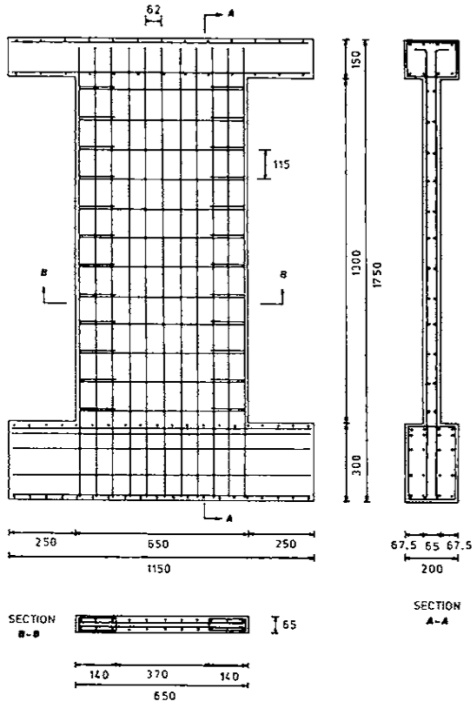

Figure 4.1: *Reinforced concrete structural wall as presented by Lefas et al. 1990 [14]*

4.1.2 Material Parameters

The concrete cube strength f_{cu} was reported as 42.8 MPa at the day of testing. The corresponding cylinder compressive strength was given as $f_{cm} = 0.85 f_{cu} = 36.4$ MPa. Strength parameters for the reinforcement steel are given in table 4.1.

Table 4.1: *Reinforcement strength parameters*

	Yield strength [MPa]	**Ultimate strength [MPa]**
Vertical reinforcement	470	565
Horizontal reinforcement	520	610
Stirrups	420	490

4.1.3 Measured Results

The article presents some interesting results, such as an unsignificant increase in shear strength when horizontal web reinforcement is present. A finding that strongly contradicts the behavior predicted by the ACI Building Code. Also, measurements of large crack widths for near ultimate loading indicated that the shear resistance due to aggregate interlock was negligible. It was concluded that the shear resistance was most likely caused by a triaxial stress condition developing in the compressive zone along the bottom edge of the wall, and that the shear stresses are carried through this zone and into the wall base. As shown in section 2.1.2 the compressive strength of concrete can be significantly increased when lateral compressive stresses are present. According to Lefas et al. the confining pressure in the compressive zone of the wall was caused by the stirrup reinforcement in the wall columns, which prohibited the volumetric expansion of the concrete for high load levels. Strain measurements showed that the tensile reinforcement underwent considerable plastic deformations prior to yielding, but failure of the reinforcement was never reached. Thus the failure of the wall was determined by the strength of the concrete in the compressive zone, rather than the strength of the reinforcement in the tensile zone.

4.1.4 Crack Patterns

Cracks first appeared as flexural cracks, along the edge of the tensile zone near the bottom right of the wall, when the applied load was about 10% of the ultimate value. When the loading was increased, these cracks propagated towards the compressive zone on the left side of the wall, gradually inclining towards the bottom left corner. The first inclined cracks were visible at a load level of about 60%. Both the flexural cracks and the inclined cracks spread towards the compressive side of the wall. When a load level of about 80% was reached, the crack pattern was fully developed and did not change noticeably until splitting was observed. Failure was caused by splitting of the compressive zone.

4.2 Element Sizes

Before conducting the NLFEAs it was necessary to establish an understanding of the differences between the medium and large scale analyses. When analyzing a non-homogenous composite material like reinforced concrete, the structural form and size is not the only factor to take into account when determining the element sizes. The element size affects the way certain material characteristics are modeled. To distinguish the difference of the element size scales, a consideration of the material composition of concrete, and the interaction between the concrete and the reinforcement was done. Then, preliminary analyses of the structural wall in question was performed in order to determine the element sizes for the medium and large scale analyses of the wall explicitly.

4.2.1 Element Size Scales

Element sizes for analysis of reinforced concrete can be divided into three scales: Rib, bar and member scale as illustrated in figure 4.2 [4]. The scale sizes can not be explicitly determined in terms of element size for structures in general. To distinguish between them, the problem at hand must be taken into account. In general, element sizes in the order of magnitude of the ribs on the reinforcement bars belong to the rib scale, sizes in the order of magnitude of the reinforcement diameter belong to the bar scale, and sizes in the order of magnitude of the structural member belong to the member scale. In this thesis the analyses are performed at two different scales, referred to as medium and large scale. These scales belong to the bar and member scales, respectively. When distinguishing between the element size scales, two subjects will be taken into account, correct representation of the tension stiffening effect discussed in section 2.1.6 and 2.2.8, and whether or not the concrete can be idealized as a homogenous material.

At rib (small) scale the interaction between concrete and reinforcement is modeled explicitly. The element size is small enough to model the ribs on the reinforcement bars and perfect bond is assumed. The concrete is modeled with tension softening. In this way the tension stiffening effect is modeled properly. Elements of this scale are often significantly smaller than the largest aggregate size in the concrete and the concrete can not be idealized as a homogenous material. Rib scale is most suited for highly detailed analysis of small specimens of reinforced concrete and the element size is unsuitable for analyses of entire structures. It is therefore outside the scope of this thesis and will not be considered in the analyses presented here.

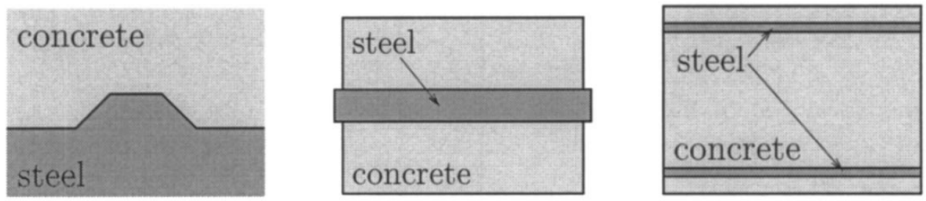

(a) *Rib (small) scale* **(b)** *Bar (medium) scale* **(c)** *Member (large) scale*

Figure 4.2: *Element size scales [22]*

For analyses of larger specimens of concrete, the medium scale is much more convenient. At this scale, the explicit modeling of the ribs of the reinforcement bars is replaced by a bond slip model. Together with a tension softening model for the concrete, the tension stiffening effect is taken into account while still securing that no stresses from the concrete are transferred at the point of yielding. In other words, the capacity is not increased. In general, a small element size is desired since it allows for detailed modeling of the structure and the possibility of obtaining localized crack patterns. However, the element size is bounded by the idea of idealizing concrete as a homogenous material. The smallest justifiable element size can be determined as three times the size of the largest aggregate in the concrete mix. Element sizes above this limit covers a large enough area of the concrete to safely describe it as homogenous [23, 11]. Lefas et al. does not report the maximum aggregate size for the concrete mix used in the structural wall experiments. However, it is reported that the mix contains 10 mm aggregate. A maximum aggregate size of 20 mm seems like a conservative assumption, and consequently a minimum element size of 60 x 60 mm is necessary for the medium scale analyses.

The transition between medium and large scale is not clearly defined. However, when the element sizes are in the order of magnitude of the structural size, they belong to the large scale. In analyses of larger concrete structures, the size of the elements no longer justifies the description of a local interaction between concrete and reinforcement, and a bond slip model should not be used. The local stiffness contributions from concrete in between fully developed cracks cannot be properly captured when the distance across an element is larger than the crack spacing. Thus, perfect bond should be specified for analyses at large scale. To account for the tension stiffening effect, a tension softening model can be used in combination with a modified crack bandwidth, limited by the crack spacing calculated for the structure. The crack bandwidth governs the width over which the stiffness contribution of the concrete is found, i.e. the width

over which a macrocrack is spread, which is limited by the crack spacing. It is reminded that a proper description of the tension softening effect is not that important in analysis of structures in a design process (cf. section 2.1.4). The element size at large scale is upper bounded by the structural behavior. It must be secured that the FE mesh is capable of reproducing the behavior with sufficient accuracy. Thus, to determine the upper bound of the element size preliminary analyses of the structure should be performed.

4.2.2 Preliminary Analyses

To find the bounds of the element sizes explicitly, preliminary linear analyses were performed. The preliminary analyses were used to determine the largest element size that produced results with sufficient accuracy, for the given geometry. If a desired behavior is to be expected in the NLFEAs, the element sizes must yield accurate results in the LFEAs. In the preliminary analyses, the structural wall was modeled without the top and bottom beams, and no reinforcement was included. To verify the results of the preliminary analyses simple hand calculations were performed. The wall was simplified as a cantilever beam subjected to a point load of 100 kN at the end as shown in figure 4.3. In the finite element model the load was applied as evenly distributed along the top edge. Youngs modulus was set to 30000 MPa. The displacement at the point of loading was calculated using shear and bending stiffness, as shown in formula (4.1).

$$\delta = F\left(\frac{1}{K_b} + \frac{1}{K_s}\right) = F\left(\frac{h^3}{3EI} + \frac{3h}{EA}\right) = 1.95 \text{ mm} \tag{4.1}$$

The model was meshed with quadratic undistorted CQ16M elements, cf. section 4.3.3. Several element sizes were tested and convergence was reached for an element size of 130 x 130 mm with reduced integration. Smaller element dimensions showed identical results. The largest element size was 650 x 650 mm, i.e. only two elements were used to mesh the model. The most notable results from the analyses are shown in table 4.2.

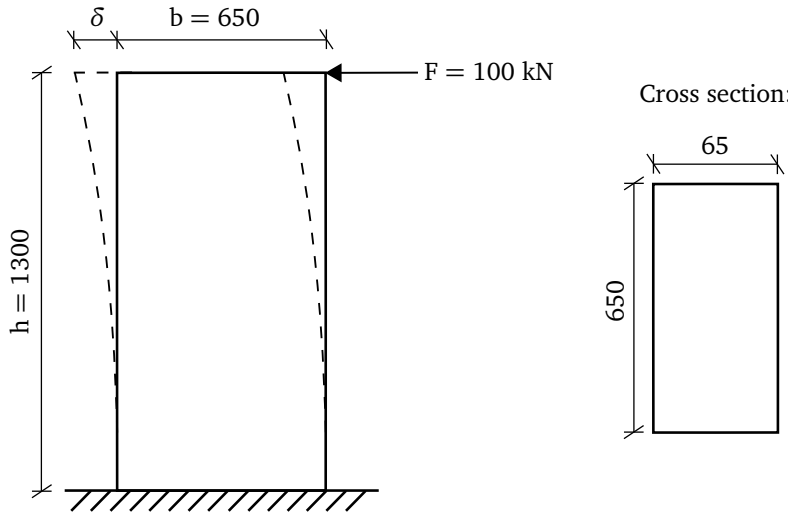

Figure 4.3: *Cantilever beam subjected to a point load*

Table 4.2: *Predicted horizontal displacement using different element sizes*

	δ[mm]	
Element size [mm]	Reduced integration	Full integration
650 x 650	1.85	1.84
325 x 325	1.90	1.89
130 x 130	1.91	1.90
65 x 65	1.91	1.91
32.5 x 32.5	1.91	1.91

The converged results in table 4.2 shows only 2.1% deviation from the calculated displacement in formula (4.1). An acceptable deviation that indicates that the finite element model behaves as desired. As expected, the finite element model predicts a smaller displacement than the hand calculations, due to the generally stiff behavior of finite elements caused by element interpolation functions that enforce an unnatural displacement field in the structure. In the medium scale analyses, an element size of 65 x 65 mm will be used. The results for 325 x 325 mm elements with reduced integration are satisfactory, and this element size will be used in the large scale analyses. Element dimensions above this limit will cause unsatisfactory results in the linear analysis and consequently also unsatisfactory results in the non-linear analyses. The element sizes for medium and large scale are both in agreement with the element size scale limits determined in section 4.2.1. The results in table 4.2 show very small deviations in the results between full and reduced integration, a good sign given that reduced integration will be used to ensure computationally effective solution of the non-linear analyses.

4.3 Finite Element Model

The finite element program DIANA, version 9.4.4, was used for creating and analyzing all finite element models presented. The program offers an extensive range of material models and is widely used for detailed finite element analyses of concrete. Some challenges were met when performing the analyses for this thesis and a chosen few of these problems are presented in more detail in appendix B. The appendix is of use for readers planning on future analyses using the DIANA finite element program.

4.3.1 Geometry, Loading and Boundary Conditions

As reported in section 4.1.1, the structural wall exhibits only in-plane displacements and it was therefore assumed that 2D-modeling was sufficient. The wall geometry was initially modeled according to the figure presented by Lefas et al., see figure 4.1, but due to several complications the model was later simplified. A description of all the finite element model generations and the corresponding complications met can be found in appendix A. The final outcome of the modeling process was two separate models for the medium and large scale analyses, as shown in figure 4.4. The concrete in the medium scale model was extended below the fixed wall base to allow for proper anchoring of the vertical reinforcement when bond slip was included. The height of the extended area corresponds to the height of the bottom beam used in the experimental tests, as seen in figure 4.1. The extended concrete does not affect the deformations of the wall above the fixed wall base. As the large scale model was analyzed without bond slip an extension below the wall base was not necessary in that model, as shown in figure 4.4(b). The dimensions and thickness of both the top beam and the wall was set according to the information from figure 4.1. All nodes along the wall base were restrained against displacements in the horizontal and vertical directions as indicated by the T-shaped anchors in figure 4.4. The existence of a fixed wall base was confirmed through measurements by Lefas et al. as described in section 4.1.1. Figure 4.4 also shows how the loading was applied as an evenly distributed load along the right edge of the top beam. The figure only shows the loading applied to the mid-side nodes of the elements on the load application edge. This is simply a consequence of the way the loading is displayed in DIANA, the load was indeed applied to all nodes along this edge. The load application in the finite element models complies with the load application reported by Lefas et al.

Reinforcement was modeled explicitly according to the information in figure 4.1. The layout of the reinforcement used in both the medium and large scale models is shown in figure 4.5. Notice the anchoring of the vertical reinforcement in figure 4.5(a).

The reinforcement bars are extended below the wall base, situated just below the bottom horizontal reinforcement bar, and bent to the outer edges of the wall. One implication of the modeling of the wall in 2D is the missing out-of-plane stirrup reinforcement in the wall columns and the top beam. This could be a limiting factor of the modeling of the triaxial stress state reported in the compressive zone.

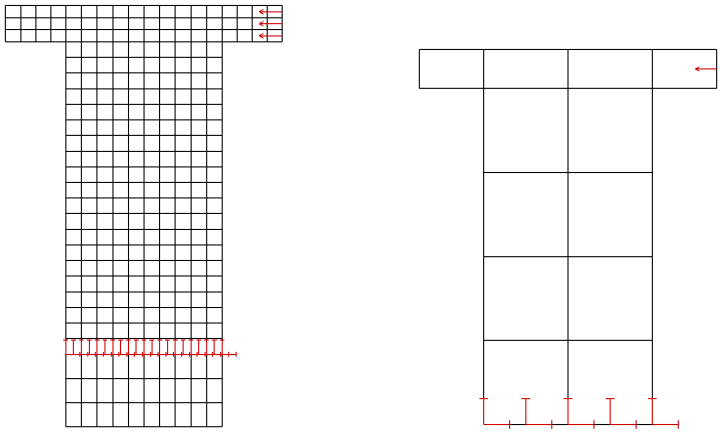

(a) *Medium scale*
65 x 65 mm elements

(b) *Large scale*
325 x 325 mm elements

Figure 4.4: *Element mesh, boundary conditions and applied load*

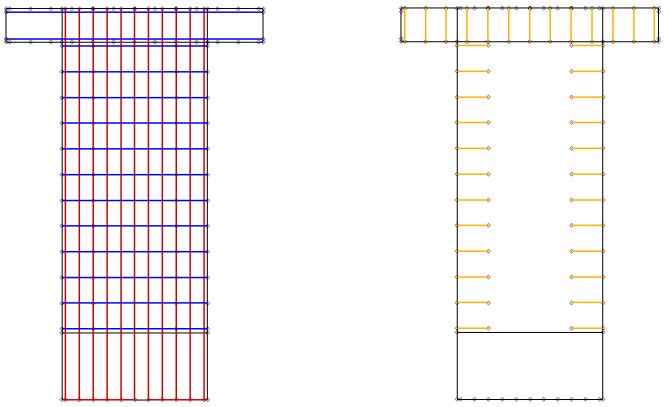

(a) *Vertical (red) and horizontal (blue) reinforcement*

(b) *Web reinforcement and top beam vertical reinforcement*

Figure 4.5: *Reinforcement layout*

4.3.2 Iterative Solution Algorithm

A Crisfield Quasi-Newton iterative solution method was used for solving all analyses [17]. To speed up convergence, the size of the incremental displacements were determined using a Line Search algorithm, and in order to pass critical points, a Spherical Arc-Length method was used. Two convergence criteria were specified, a residual force criterion and an energy criterion with convergence tolerances of 10^{-2} and 10^{-4}, respectively.

4.3.3 Element Types

The element chosen was CQ16M, a quadrilateral plane stress element with eight nodes, shown in figure 4.6. The element is based on quadratic interpolation and reduced Gauss integration is used to calculate stresses and strains [17]. Reduced integration of the element is obtained by using 2 x 2 integration points. A default crack bandwidth $h = \sqrt{A}$, where A is the area of the element, is calculated in DIANA unless a constant crack bandwidth is specified [17].

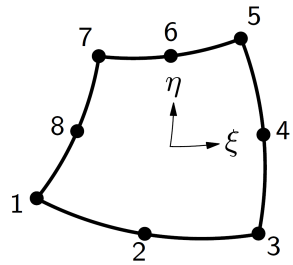

Figure 4.6: *The CQ16M quadrilateral eight node plane stress element*

The reinforcement was modeled explicitly using the CL6TR truss element, shown in figure 4.7(a). The element is 3-noded and the strains and stresses are purely axial, i.e. the element has no shear stiffness nor any flexural rigidity. A 2-point Gauss integration scheme is used for the element. Stresses and strains in the reinforcement are transferred to the concrete through the nodes of the concrete element surrounding each reinforcement truss element. For implementation of bond slip, the CQ22IF element, shown in figure 4.7(b), was used as a link between the concrete elements and the reinforcement elements. The element handles the relative slip, and the transfer of traction stresses between the concrete and reinforcement elements.

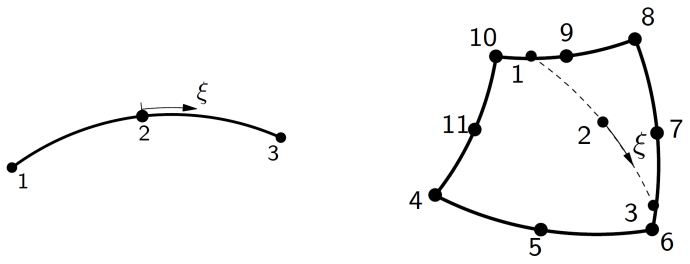

(a) *CL6TR truss element* **(b)** *CQ22IF interface element*

Figure 4.7: *Elements used for modeling of reinforcement*

4.4 Material Parameters

When performing the NLFEAs, the intended use in a design process as suggested in section 3.2 was kept in mind. Thus, parametric studies of material parameters were not of interest. The material parameters were determined as they would be in a design process and the variability of the output from the analyses is due to changes in the solution strategy alone.

4.4.1 Crack Spacing

As stated in section 2.2.1 and 4.2.1, an element size larger than the crack spacing makes the use of an adjusted crack bandwidth necessary. This crack bandwidth can be set equal to an estimated crack spacing in the structure. The crack spacing in the direction of both reinforcement layers was therefore calculated according *fib* Model Code 2010 [20]. The maximum crack spacing is calculated according to formula (4.2), where k was set to 1.0, c is the concrete cover, $\tau_{bm} = 1.8 f_{ctm}$ is the mean bond strength between steel and concrete, ϕ_s is the diameter of the reinforcement bars and $\rho_{s,eff}$ is the ratio between the reinforcement area and the effective concrete area.

$$l_{s,max} = 2\left(k \cdot c + \frac{1}{4}\frac{f_{ctm}}{\tau_{bms}}\frac{\phi_s}{\rho_{s,eff}}\right) \tag{4.2}$$

For an element in pure tension, the crack will develop orthogonal to the direction of the applied force and the maximum crack spacing calculated in that direction can be used as a measure of the crack bandwidth. For an element in an arbitrary state of stress, as shown in figure 4.8(a), the crack will develop at an angle and the crack

spacing is calculated on basis of the crack spacing in the x- and y-directions, and the crack angle. The crack angle can be found by taking into account the stress state of the element and the reinforcement forces in all directions. The Compendium for Concrete Structures 3 [24], a subject offered at NTNU, states three possible ways of finding the crack angle. The structural wall investigated has unequal reinforcement amounts in the x- and y-directions and thus only alternative 2 and 3 are relevant. Alternative 2, shown in formula (4.3), assumes yielding of the reinforcement in both directions. Alternative 3, shown in formula (4.4), assumes initial yielding in one reinforcement direction, it also assumes linear behavior of the reinforcement and disregards the tensile strength of the concrete. When the crack angle has been found, the maximum crack spacing can be calculated using formula (4.5).

$$\text{Alt. 2:} \qquad \tan^2(\theta) + \left(\frac{N_x}{N_{xy}} - \frac{N_y}{N_{xy}} \frac{A_{sx}}{A_{sy}} \right) \cdot \tan(\theta) - \frac{A_{sx}}{A_{sy}} = 0 \tag{4.3}$$

$$\text{Alt. 3:} \qquad \tan^4(\theta) + \frac{N_x}{N_{xy}} \cdot \tan^3(\theta) - \frac{N_y}{N_{xy}} \frac{A_{sx}}{A_{sy}} \cdot \tan(\theta) - \frac{A_{sx}}{A_{sy}} = 0 \tag{4.4}$$

$$l_{s,max}(\theta) = \left(\frac{\cos\theta}{l_{s,max,x}} + \frac{\sin\theta}{l_{s,max,y}} \right)^{-1} \tag{4.5}$$

Using formulas (4.2) through (4.5), the maximum crack spacing of the structural wall investigated in this thesis was calculated. It is evident that the wall will have zones where the stress state is dominated by shear stresses and the crack angle is therefore of interest. As a simplification, the crack angle was determined for an element of the wall subjected to pure shear ($N_x = N_y = 0$). The element reinforcement ratios in the x- and y-directions were accounted for by means of the reinforcement cross sectional areas and the distance between the reinforcement bars, s_x and s_y. The element in question is illustrated in figure 4.8(b). Results from the calculations are summarized in table 4.3. Although the results from the shear wall experiments reveals that the vertical reinforcement yields first, in agreement with formula (4.4), this would not be straight forward to calculate for all areas of a large concrete structure in a design process. Thus the crack spacing was determined as the mean of the calculated values for alternative 2 and 3 in table 4.3: $\bar{l}_{s,max} = 88$ mm. Notice that this crack spacing is

smaller than the element dimensions in the large scale analyses. Thus, the automatic bandwidth calculated in DIANA must be modified to secure energy-equivalency of the fracture process (cf. section 2.2.1), and to properly account for the tension stiffening effect (cf. section 4.2.1). The modification is done by scaling the fracture energy as shown in section 4.4.2.

Table 4.3: *Results from calculation of crack spacing*

	Crack angle θ	**Maximum crack spacing [mm]**
x-direction	-	136
y-direcion	-	105
Alt. 2	29.8°	90
Alt. 3	37.1°	86

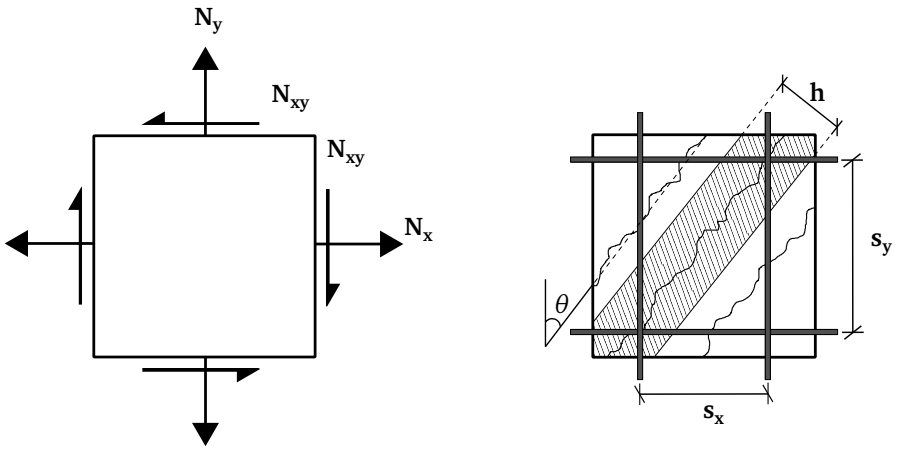

(a) *External forces* **(b)** *Crack bandwidth h and crack angle θ*

Figure 4.8: *Determination of crack bandwidth*

4.4.2 Strength Parameters

The Dutch guidelines that were used as a basis for selecting the material models in section 2.2 was also used as a reference for obtaining the material properties needed for the NLFEAs. As described in the guidelines, most material properties of concrete can be derived from the characteristic cylinder compressive strength. Relevant calculated material properties for the analyses are given in table 4.4, where the mean compressive strength f_{cm} is as reported in section 4.1.2.

Table 4.4: *Basic strength parameters of concrete*

Mean compressive strength:	f_{cm}	=	36.4 MPa
Characteristic compressive strength:	$f_{ck} = f_{cm} - \Delta f$	=	28.4 MPa
Mean tensile strength:	$f_t = f_{ctm} = f_{ctk0,m}\left(\frac{f_{ck}}{f_{ck0}}\right)^{2/3}$	=	2.8 MPa
Constants:	Δf	=	8 MPa
	$f_{ctk0,m}$	=	1.4 MPa
	f_{ck0}	=	10 MPa

The modulus of elasticity was calculated to 33.1×10^3 MPa according to *fib* Model Code 2010 [20] (formula (4.6)).

$$E_{ci} = E_{c0} \cdot \alpha_E \cdot \left(\frac{f_{cm}}{10}\right)^{1/3} \tag{4.6}$$

where:
$E_{c0} = 21.5\times10^3$ MPa
$\alpha_E = 1.0$

The Dutch guidelines state that the fracture energy is dependent upon the maximum aggregate size. The concrete used in the structural wall experiments performed by Lefas et al. was reported to contain an amount of 10 mm aggregate 3.15 times the weight of cement. The report does not give any more information about the aggregate size in the concrete used. It was therefore assumed that the maximum aggregate size was bounded by a diameter of 16 mm which gives a fracture energy G_F of 0.074 Nmm/mm^2 (formula (4.7)). This limit was chosen simply because the Dutch guidelines lists possible values for the fracture energy based on maximum aggregate sizes of 8, 16 and 32 mm,

and an aggregate size of 32 mm seemed unreasonable. The fracture energy of concrete in compression was set to $G_C = 250G_F$.

$$G_F = G_{F0}\left(\frac{f_{cm}}{f_{cm0}}\right)^{0.7} \tag{4.7}$$

where:
$G_{F0} = 0.030$ Nmm/mm^2 for a maximum aggregate size of 16 mm
$f_{cm0} = 10$ MPa

As found in section 4.4.1 the element dimensions of the large scale analyses makes it necessary to manipulate the crack bandwidth in DIANA. However, if the crack bandwidth is modified directly, the compression response will also be affected, because it depends on the same crack bandwidth, see figure 2.8. Instead, a scaled fracture energy $\overline{G}_F$ in tension is found according to the crack spacing calculated in section 4.4.1, and the automatic crack bandwidth calculated in DIANA for the large scale analyses. Formula (4.8) shows how this scaling was done, where h represents the crack bandwidth calculated in DIANA.

$$\overline{G}_F = \frac{h}{l_{s,max}} G_F \tag{4.8}$$

4.5 Results From NLFEA

In this section the results from all NLFEAs are presented. In the review of the results, the crack terminology presented in figure 4.9(a) will be used. Where colored contour plots of tensile strains are presented the values are referring to strain values as illustrated in figure 4.9(b), the color values will also be presented in a legend-plot along with the figures. Presented figures that are not self-explanatory will be accompanied by a short description. Results are mainly presented from converged load steps, if non-converged results are presented it will be specified. In general, the load step numbered with an X represents the first non-converged load step after the maximum capacity of an analysis is reached. The amount of output data from the analyses is immense and only a small selection of the available data is presented here. However, the presented data should give a more detailed view of the stress-state in the structural wall during loading, and help identify the cause of failure.

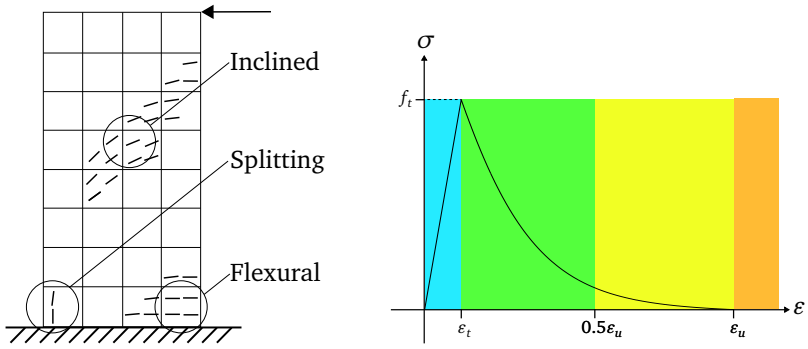

(a) *Different crack types* **(b)** *Contour levels for concrete*

Figure 4.9: *Explanatory figures for interpretation of results*

4.5.1 Medium Scale Analyses

Figure 4.10 shows the load-deflection curves for the medium scale analyses. The figure also specifies two important stages of the deformational response, initiation of flexural cracking and first yield of the vertical tension reinforcement. Both crack models correlate well with the experimental data until an external load of about 80 kN is reached. At this point the maximum capacity is reached for the rotating crack model and the load-carrying capacity of the wall is quickly reduced. The fixed crack model reaches its maximum capacity of 91 kN at a deflection of about 23 mm. Initiation of flexural cracking occurs at 12 kN for both models, a load level that is in agreement with the

reported value from the experiment of 13 kN. For both analyses yielding takes place after the first peak in the load-deflection curve, the fixed and rotating crack models display yielding at 73 and 48 kN, respectively. The experimental load at yielding was reported as 80 kN.

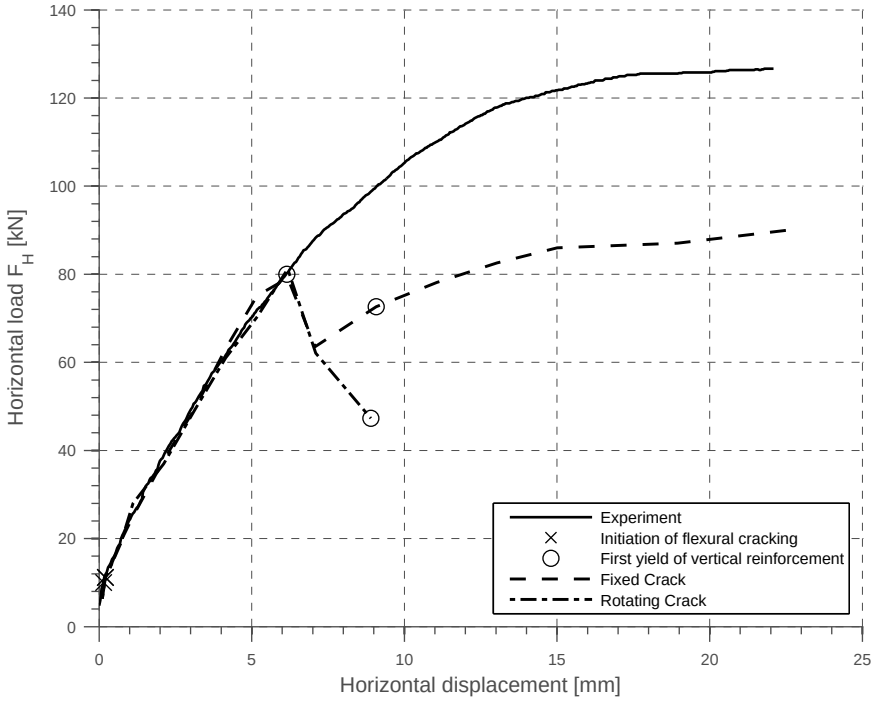

Figure 4.10: *Load-deflection curves for medium scale analyses*

Figures 4.11 and 4.13 show how the depth of the neutral axis is gradually decreasing as the external load is applied. The zoomed in plots display the crossing point of the strain curves in more detail. In both the fixed and the rotating crack analyses a minimum depth of about 100 mm is observed at the initial peak load. After the initial peak load is reached, both analyses display a shift of the position of the neutral axis as shown in figures 4.12 and 4.14, the compressive zone is expanded. The height of the compressive zone after the shift is 205 mm for the fixed crack model and 190 mm for the rotating crack model. Notice that load step X in figure 4.14 did not converge. However, the values of the residual force in this step was of a magnitude that indicate that the solution is not far from a converged one. The strains from the load step is reported here to give an indication of the shift of the compressive zone.

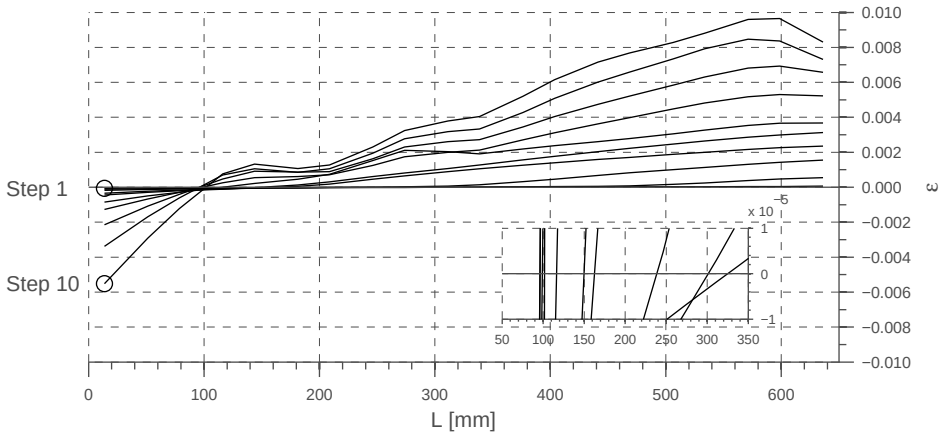

Figure 4.11: *Strain along wall base in the fixed crack model - Load steps 1 to 10*

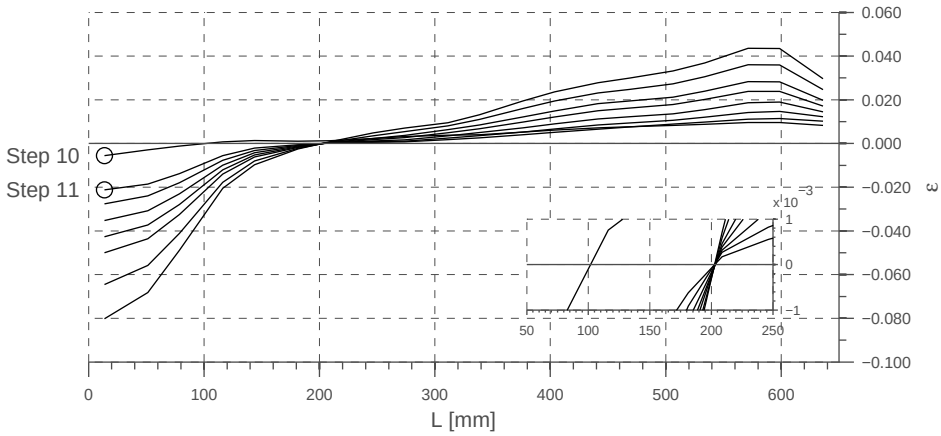

Figure 4.12: *Strain along wall base in the fixed crack model - Load steps 10 to 17*

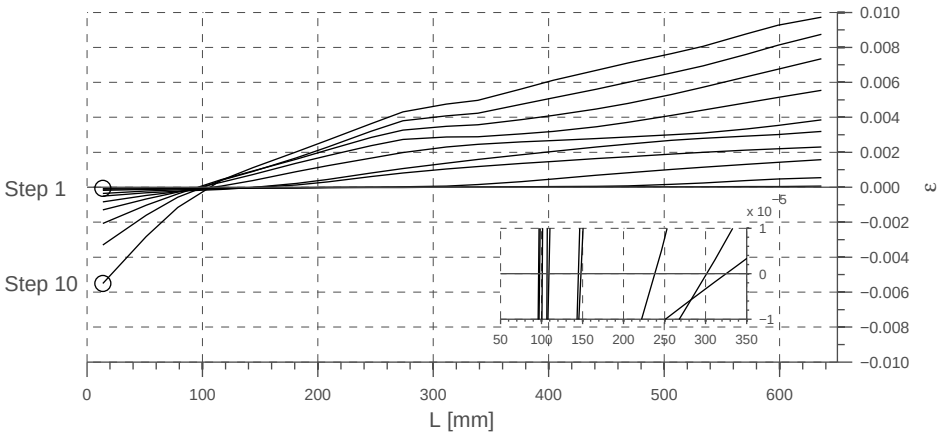

Figure 4.13: *Strain along wall base in the rotating crack model - Load steps 1 to 10*

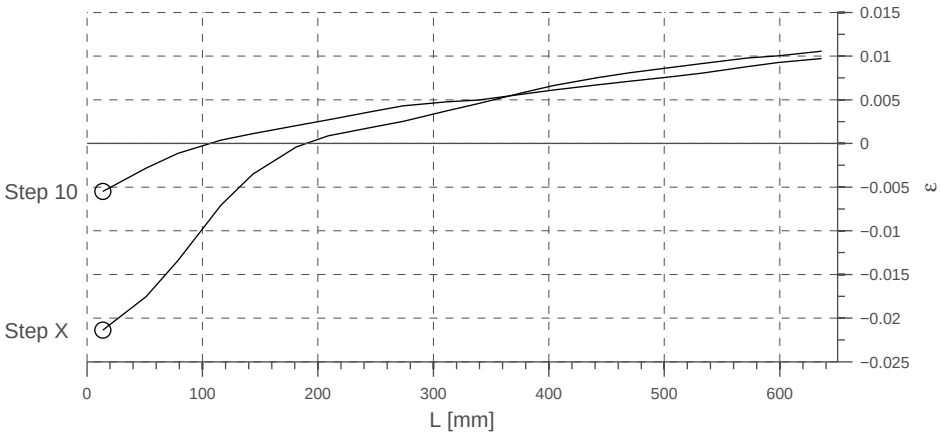

Figure 4.14: *Strain along wall base in the rotating crack model - Load steps 10 to X*

Figures 4.15 and 4.16 offer a comprehensive overview of the analysis results. The figures contain a lot of data and a short explanation may therefore be in order. The solid line shows the stress in the most critical vertical reinforcement bar, located on the far right of the tension zone, with values of the reinforcement stress given in the left axis. The dashed and dashed-and-dotted lines show the concrete stress in the global y-direction of the structural wall in two different integration points. The stress orientation in these integration points is nearly vertical, thus the stresses in the global y-direction should be representative for the compressive principal stresses in these points. The values presented in the figures where indeed confirmed to be in the same order of magnitude as the compressive principal stresses. The integration points 1 and 2 represent the most extreme compressive fiber of the concrete before and after the shift in the depth of the neutral axis, respectively. Values for the concrete stress is given in the right axis. Finally, the bar plot displays the applied external loading with values in kN given just below the top of the bars. The x-axis represents the load steps applied in the analyses.

Both figure 4.15 and 4.16 clearly show the shift of the compressive zone between load steps 10 and 11. During this shift the compressive stresses are transferred from the initial compressive zone fronted by integration point 1 to the new compressive zone fronted by integration point 2. Both the fixed and rotating crack models display the same behavior until this stage and the compressive stresses in integration point 1 is in the order of magnitude of the cylinder strength for both analyses before the shift occurs. Notice that both crack models show yielding of the most critical vertical reinforcement bar after the shift of the compressive zone. The fixed crack model (figure 4.15) predicts compressive stresses of about 1.6 times the uniaxial cylinder strength in integration point 2 after the shift, an indication that a considerable biaxial stress state is present. The rotating crack model (figure 4.16) does not display the same biaxial conditions for integration point 2.

Figures 4.17 and 4.18 display the crack pattern and the tensile principal strains in selected load steps. Cracks are displayed explicitly as lines while the tensile strains are displayed as contour plots. The strain values represented by the colors in the contour plots are specified in the legend shown, and in fig 4.9(b). Some of the figures indicate that cracks are present at strain levels below the crack limit, this is merely a consequence of the extrapolation method used to create the plots in DIANA. Some cracks visible in the results from the fixed crack model are orthogonal to the expected crack direction. This is caused by the way DIANA reports the cracks in an integration point where two cracks have occurred, such cracks are thus accompanied by an orthogonal crack which

is not shown. All figures are deformed according to the nodal displacements in the given load step. The displacements are multiplied by a factor of 5 to help distinct the deformations, this might yield some abnormal displacement fields in the last load steps. Figures 4.17(a) through 4.17(d), and 4.18(a) through 4.18(d), show how the crack pattern spreads out both horizontally and vertically from localized cracks initiated at the tensile edge of the wall. Eventually $^3/_4$ of the wall width is covered by a fully cracked zone. Figures 4.17(d), 4.17(e), 4.18(d) and 4.18(e) show how splitting in the compressive zone is initiated in load step 10 and significantly developed in load step 11, for both crack models. Figure 4.17(f) represents the last load step in the fixed crack analysis. As the figure shows, the crack pattern has not changed noticeably from load step 11 until the last step. Notice that figure 4.18(e) belongs to a non-converged load step. The figure is reported here to give an indication of the crack pattern after the peak load of the rotating crack model.

Figures 4.19(a) through 4.20(b) display the compressive principal stress path and the negative shear stresses in the wall elements. The stress path is displayed as vectors, with lengths illustrating the magnitude of the stress. The shear stresses in the elements are displayed as contour plots, with color values as given in the legend between the figures. The figures show how the far left element row of the wall behave as a compressive column, with an almost vertical orientation of the compressive principal stresses and an insignificant magnitude of shear stresses. It is also evident in the figures 4.19(a) and 4.20(a), displaying the situation in the last step before the shift of the compressive zone, that the expanding cracked right side of the wall does not contribute much to the shear capacity. A shear band can be seen stretching from the middle of the top edge and spreading out between the compressive column at the left and the cracked zone to the right. At the bottom of the wall, where the extent of the cracked zone in the right is at its maximum, the shear band is narrowing in towards the compressive zone, transferring the shear forces to the fixed base. The figures 4.19(b), 4.19(c) and 4.20(b) show how the compressive principal stress path is changed after the shift of the compressive zone. The capacity in the front of the initial compressive zone is drastically reduced and the stresses are drawn towards the new front of the compressive zone. The far left elements of the wall base carry no shear stresses and thus the shear band shifts towards the new front of the compressive zone. The unloading that occurs in the fixed crack model in step 11 (cf. fig 4.15), and in the rotating crack model in step X (cf. figure 4.16), is indicated by the decreased shear stresses in the shear band through the wall in figures 4.19(b) and 4.20(b). Again, load step X is not converged but reported to give an indication of the unloading process.

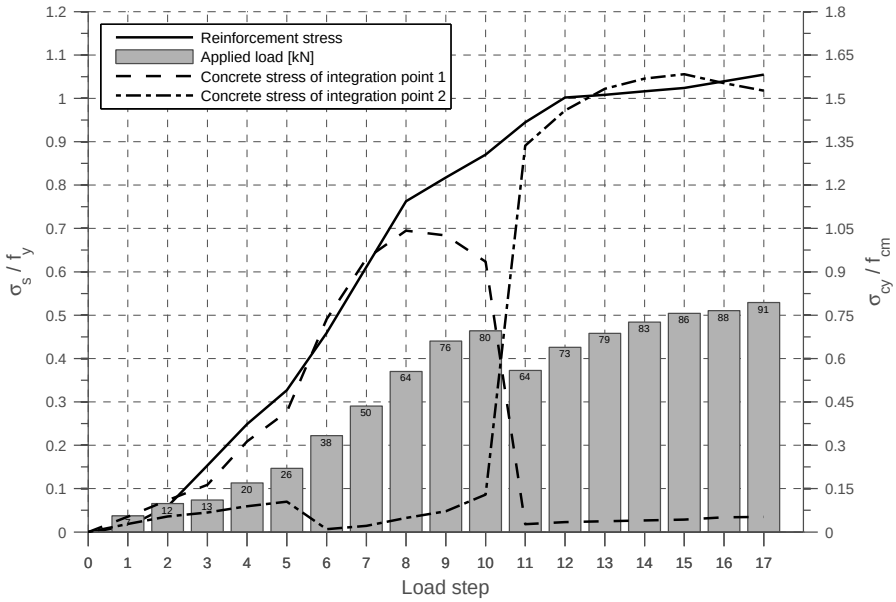

Figure 4.15: *Fixed crack model - Analysis result overview*

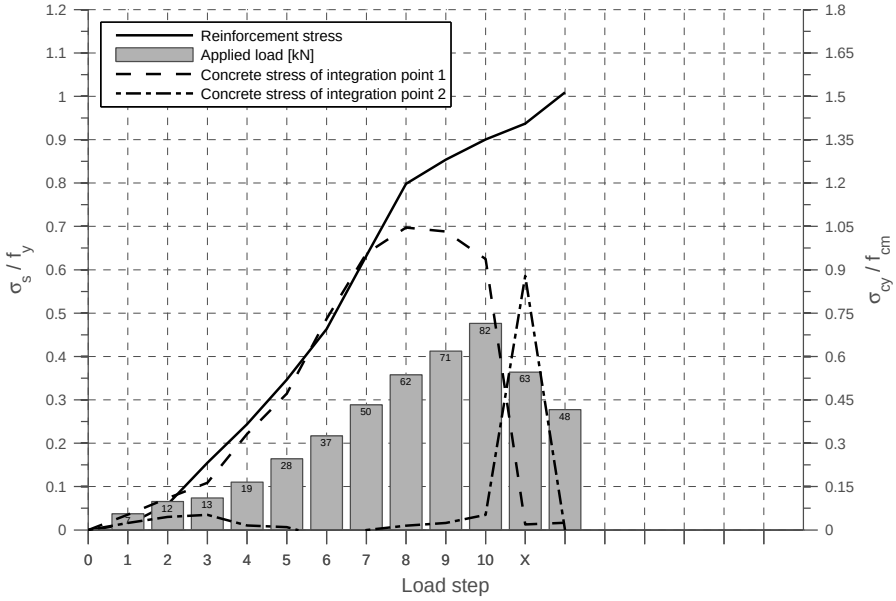

Figure 4.16: *Rotating crack model - Analysis result overview*

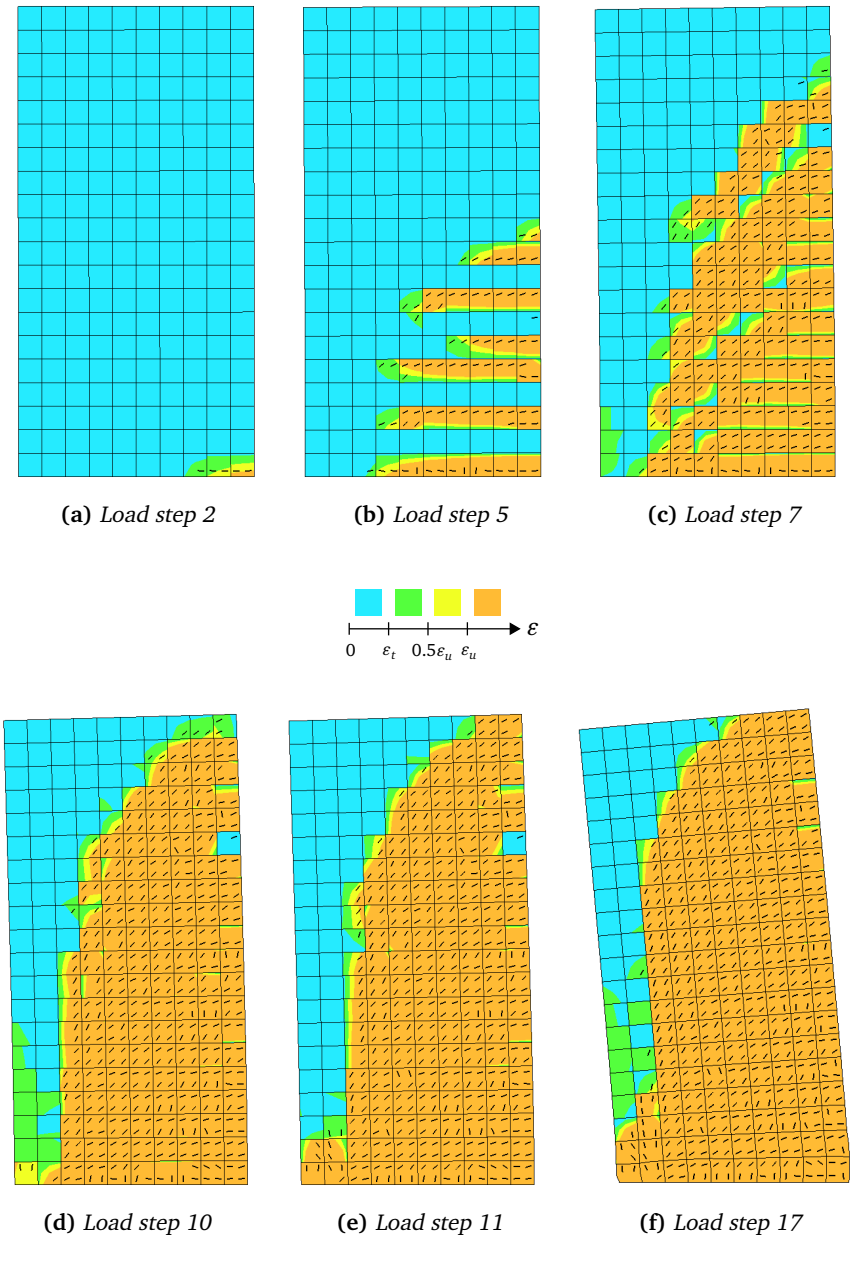

(a) *Load step 2* **(b)** *Load step 5* **(c)** *Load step 7*

(d) *Load step 10* **(e)** *Load step 11* **(f)** *Load step 17*

Figure 4.17: *Fixed crack - Crack patterns and tensile principal strain contour plots*

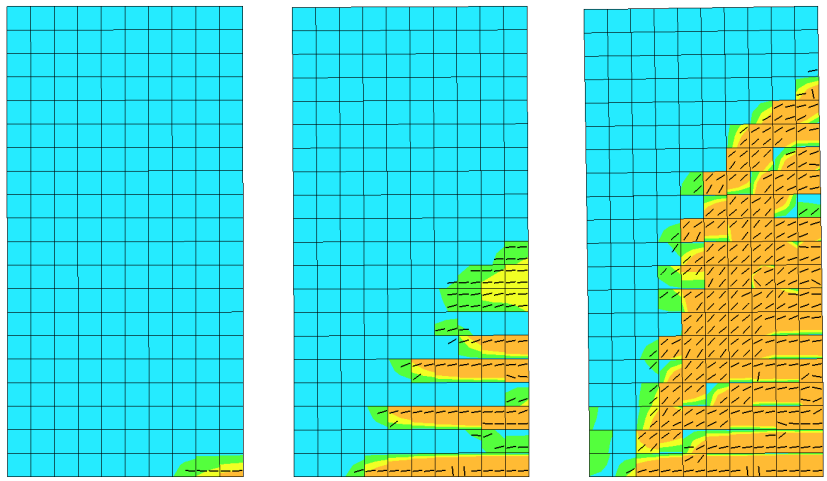

(a) *Load step 2* **(b)** *Load step 5* **(c)** *Load step 7*

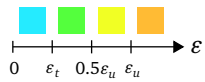

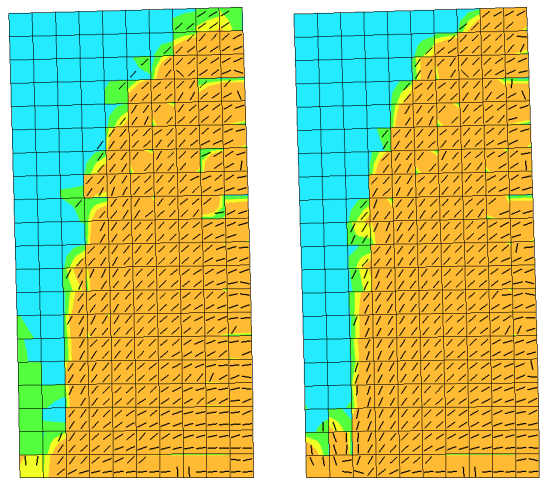

(d) *Load step 10* **(e)** *Load step X*

Figure 4.18: *Rotating crack - Crack patterns and tensile principal strain contour plots*

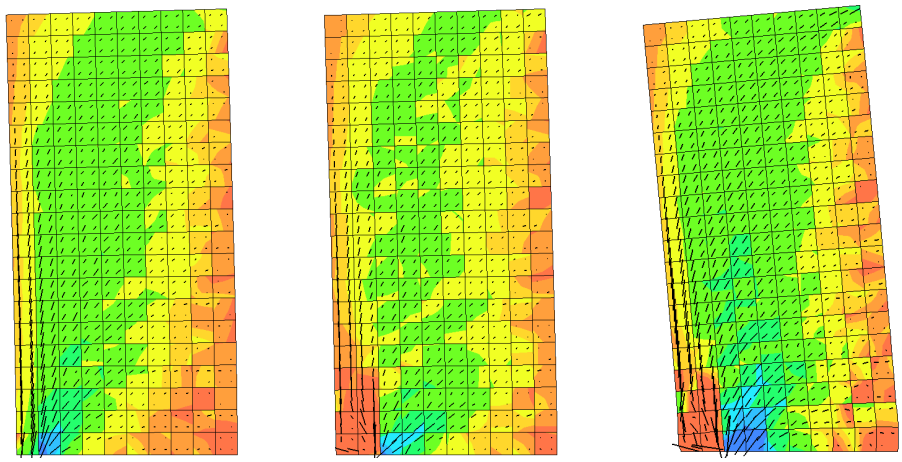

(a) *Load step 10* **(b)** *Load step 11* **(c)** *Load step 17*

Figure 4.19: *Fixed crack - Compressive principal stress path and shear stress contour plots*

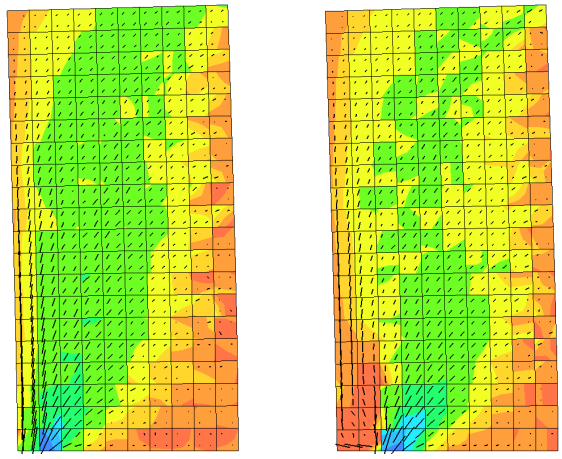

(a) *Load step 10* **(b)** *Load step X*

Figure 4.20: *Rotating crack - Compressive principal stress path and shear stress contour plots*

4.5.2 Large Scale Analyses

The load-deflection curves of the large scale analyses are shown in figure 4.21. The curves are cut off at 30 mm deflection to illustrate that no increase in capacity takes place after the initial load peak. Numerical failure is predicted at this point by the rotating crack model, while the fixed crack model would deform the structural wall until numerical divergence at 96 mm deflection. However, the ultimate capacity of the wall and the mode of failure can be described using the first 20 load steps. Thus, the following figures displaying results from the analyses will represent load steps 1 to 20. Both analyses predict the same structural behavior on a global level, and an ultimate load capacity at 83% of the experimental load capacity. Initiation of flexural cracking is observed at 17 kN for both models, somewhat above the 13 kN reported by Lefas et al. Yielding is predicted at 79 and 78 kN for the fixed and rotating crack models, respectively, compared to 80 kN reported in the experiment.

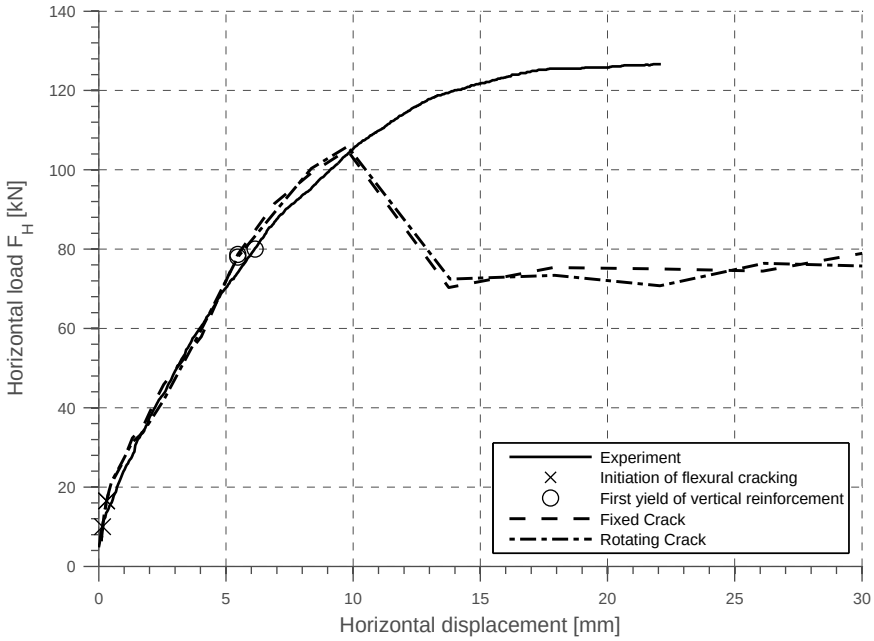

Figure 4.21: *Load-deflection curves for large scale analyses*

Figures 4.22 and 4.24 show how the compressive zone along the wall base in both the fixed and rotating crack models is gradually decreased in load steps 1 to 15, until a minimum height of about 130 mm is reached. As shown in figures 4.23 and 4.25, the

compressive zone is shifted in step 16, to a height of 275 and 250 mm for the fixed and rotating crack models, respectively.

Figures 4.26 and 4.27 illustrate the analysis with results from both the compressive (concrete) and the tensile (reinforcement) zones of the wall base. The figures show how the concrete compressive stresses are gradually increased in the compressive zone, represented by integration point 1, in load steps 1 to 15. The compressive stresses reach a level of about 0.8 times the compressive strength before unloading. In load step 16 the shift of the compressive zones lead to an increase of the compressive stresses in integration point 2. The stresses are built up to a level of about 0.16 and 0.3 times the compressive strength for the fixed and rotating crack models, respectively. Yielding of the most critical vertical reinforcement bar is initiated in load step 12 for both analyses.

Figures 4.28(a) through 4.29(f) show the crack pattern and the tensile principal strains for a selection of load steps. As seen in the other results in this section, the two crack models predict similar behavior of the structural wall in the large scale analyses. Figures 4.28(a) trough 4.28(d), and 4.29(a) through 4.29(d), show how the crack pattern is initiated in the bottom right corner of the wall and spread out both vertically and towards the left edge. Splitting of the compressive zone is evident in figures 4.28(e) and 4.29(e). Additional splitting occurs for the fixed crack model in the subsequent load steps as seen in figure 4.28(f), while figure 4.29(f) shows no changes in the crack pattern for the rotating crack model.

Figures 4.30(a) through 4.31(c) display the compressive principal stress path and the shear stresses for selected load steps. A shear band stretching from the upper right to the bottom left corner is evident in figures 4.30(a) and 4.31(a). Figures 4.30(b) and 4.31(b) show how this shear band moves toward the tensile edge of the wall as the shift of the compressive zone occurs in load step 16. The shear stresses in the most extreme right of the tensile zone are larger in the fixed than in the rotating crack model. The results from load step 20 is shown in figures 4.30(c) and 4.31(c). No significant changes occur for either the shear state of the wall or the orientation of the compressive principal stress path in either crack models, after the shift of the compressive zone.

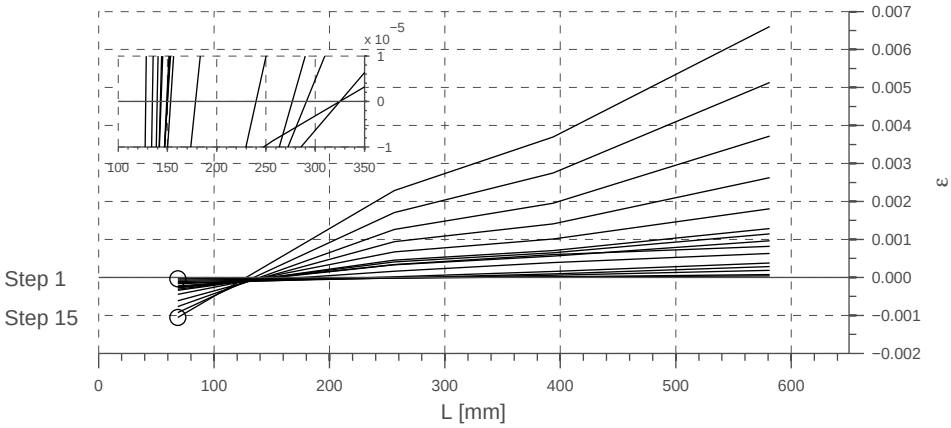

Figure 4.22: *Strain along wall base in the fixed crack model - Load steps 1 to 15*

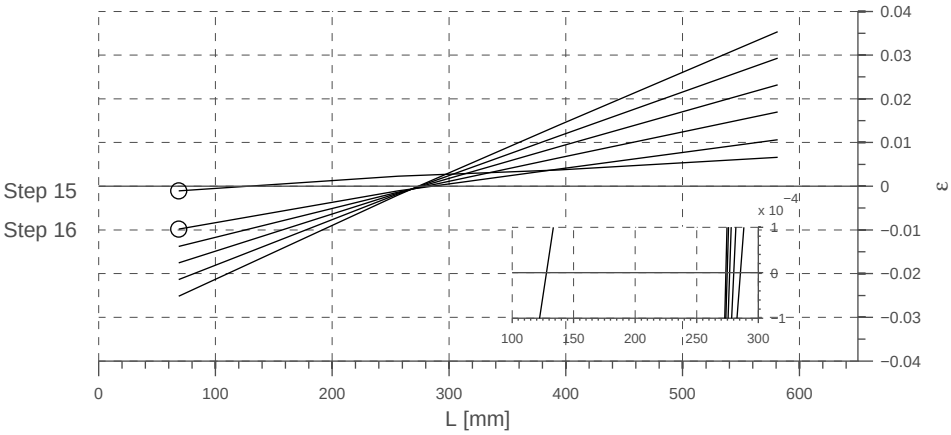

Figure 4.23: *Strain along wall base in the fixed crack model - Load steps 15 to 20*

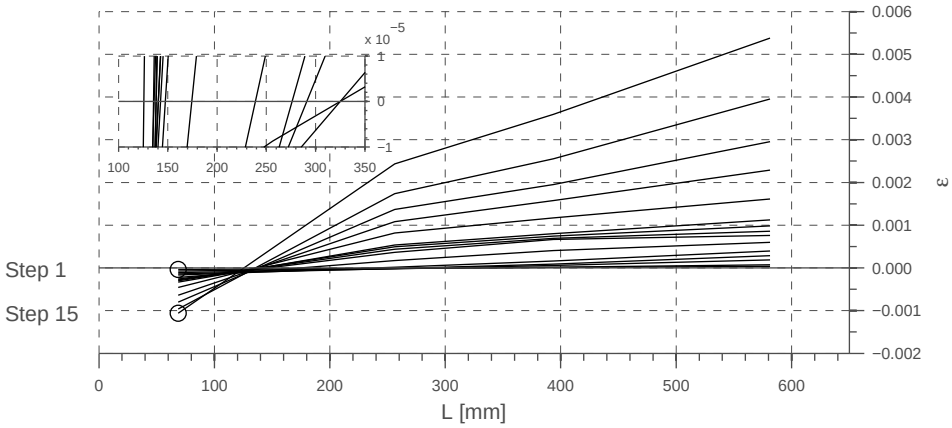

Figure 4.24: *Strain along wall base in the rotating crack model - Load steps 1 to 11*

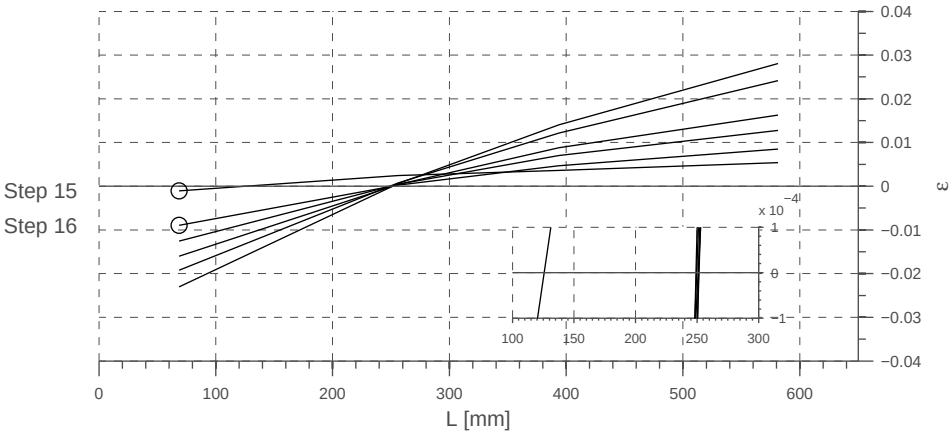

Figure 4.25: *Strain along wall base in the rotating crack model - Load steps 15 to 20*

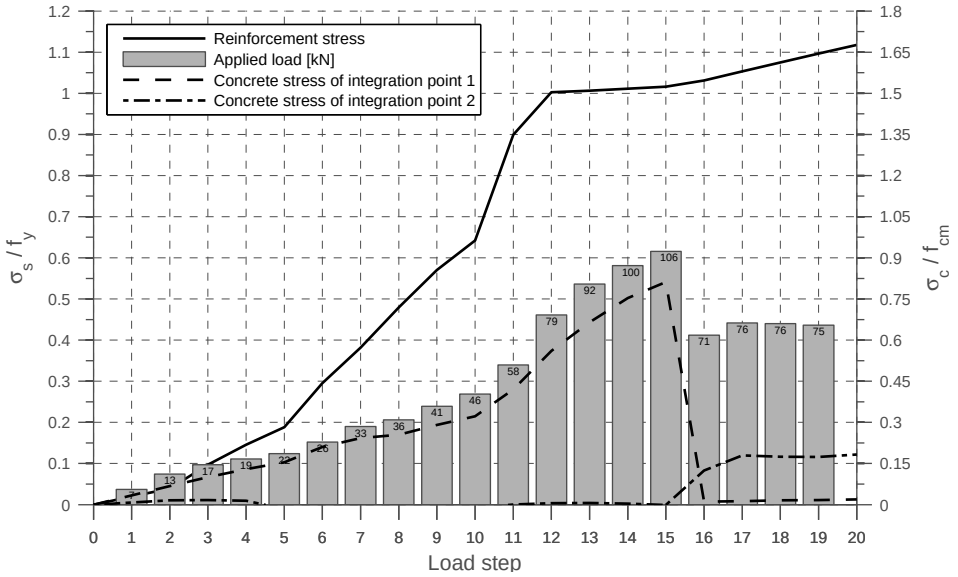

Figure 4.26: *Fixed crack model - Analysis result overview*

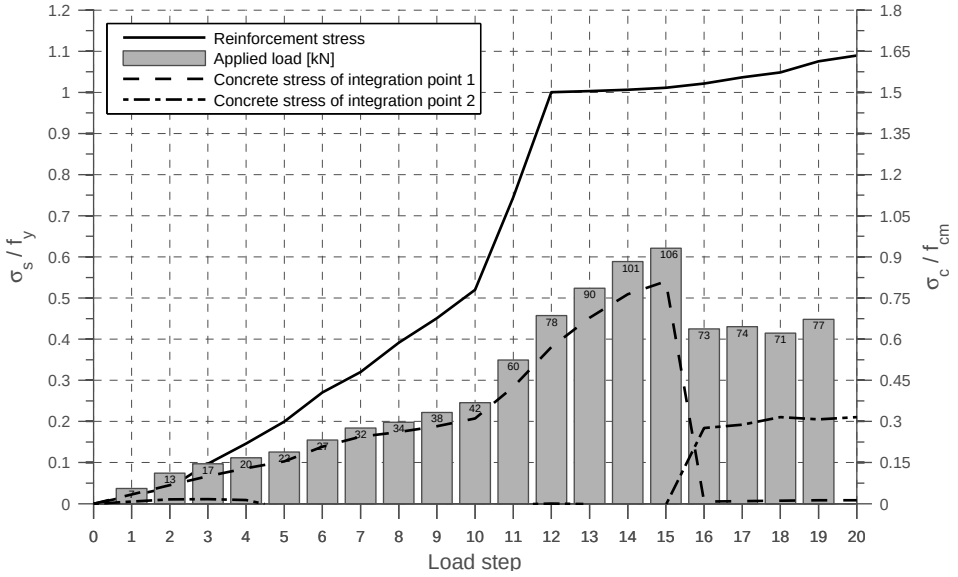

Figure 4.27: *Rotating crack model - Analysis result overview*

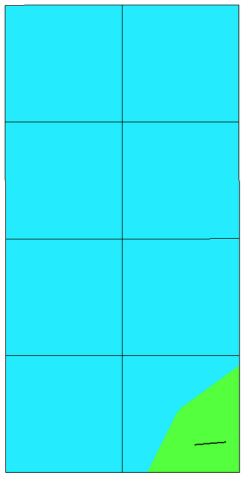

(a) *Load step 3*

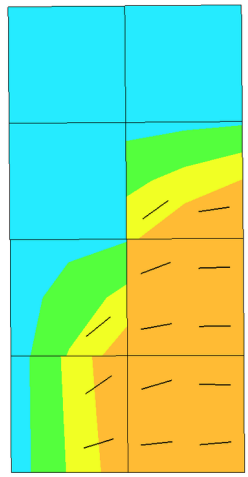

(b) *Load step 8*

(c) *Load step 12*

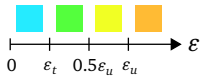

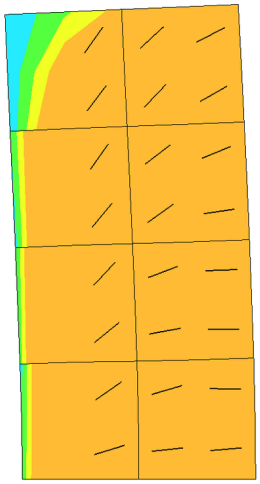

(d) *Load step 15*

(e) *Load step 16*

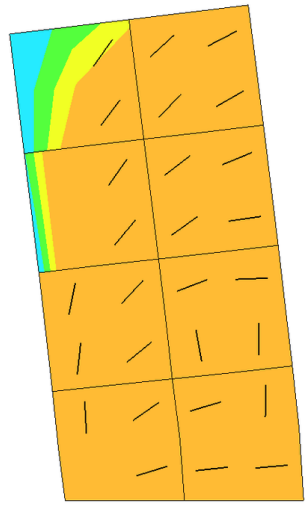

(f) *Load step 20*

Figure 4.28: *Fixed crack - Crack patterns and tensile principal strain contour plots*

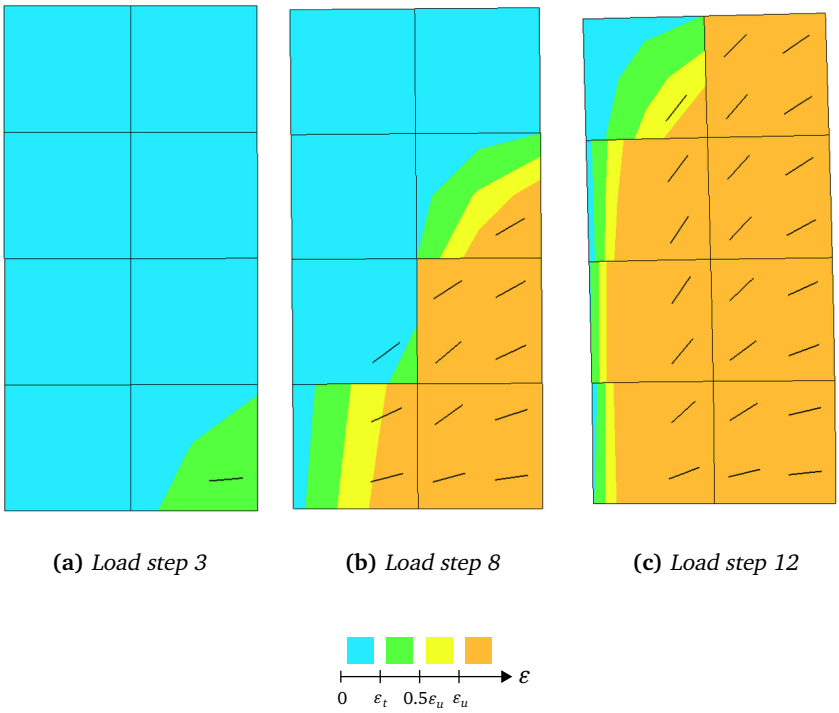

(a) *Load step 3* **(b)** *Load step 8* **(c)** *Load step 12*

(d) *Load step 15* **(e)** *Load step 16* **(f)** *Load step 20*

Figure 4.29: *Rotating crack - Crack patterns and tensile principal strain contour plots*

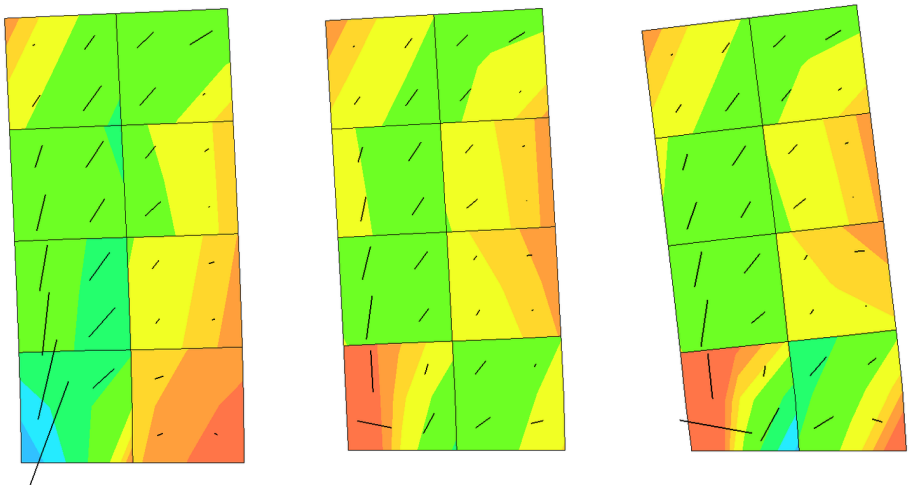

(a) *Load step 15* **(b)** *Load step 16* **(c)** *Load step 20*

Figure 4.30: *Fixed crack - Compressive principal stress path and shear stress contour plots*

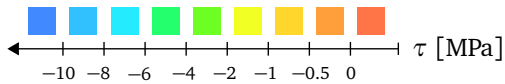

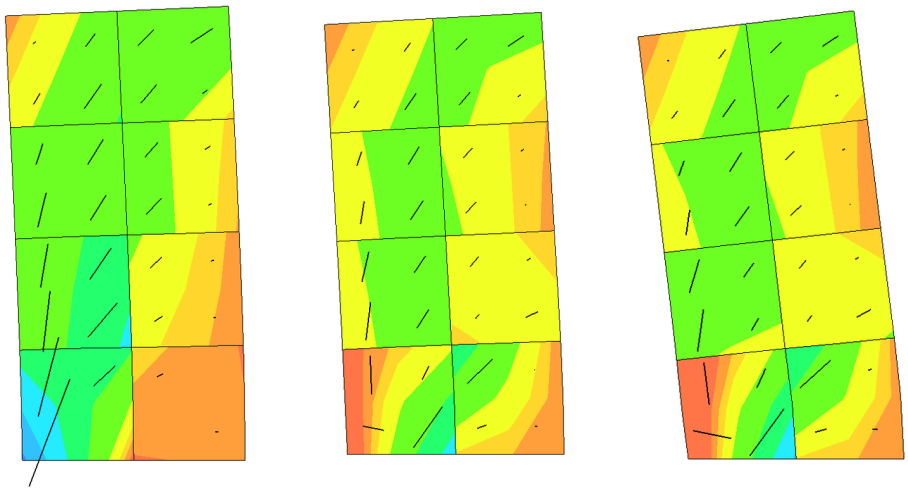

(a) *Load step 15* **(b)** *Load step 16* **(c)** *Load step 20*

Figure 4.31: *Rotating crack - Compressive principal stress path and shear stress contour plots*

4.5.3 Summary of Results

Characteristic load and deflection values are summarized in table 4.5. F_{cr} and F_Y denotes the loading at which initiation of flexural cracking and yielding of the vertical tension reinforcement was observed, respectively. $F_P(\delta_P)$ denotes the load at the initial load peak and the corresponding deflection of the wall. $F_U(\delta_U)$ denotes the ultimate load and the corresponding deflection. Load and deflection values are reported in kN and mm, respectively. The percentage of the experimentally determined values are given below the load values.

Table 4.5: *Load and deflection values from analyses*

	Medium scale		***Large scale***	
	Fixed crack	**Rotating crack**	**Fixed crack**	**Rotating crack**
F_{cr}	12 92%	12 92%	17 131%	17 131%
F_Y	73[1] 91%	48[1] 60%	79 99%	78 98%
$F_P(\delta_P)$	80(6.2) 63%	82(6.2) 65%	106(9.8) 83%	106(9.8) 83%
$F_U(\delta_U)$	91(22.9) 72%	82(6.2) 65%	106(9.8) 83%	106(9.8) 83%

[1] Yield predicted after load peak

5 Discussion

Before discussing the differences between the medium and large scale analyses, the agreement between the indivudial analyses and the experimental results will be investigated. Suggestions to improve the analysis results are given, with special attention directed at the volumetric expansion effect. Finally the effect of the element size on the analysis result is discussed both with respect to the case study performed and with respect to the proposed use in a design process as presented in chapter 3.

5.1 Medium Scale Analyses

As figure 4.10 clearly shows, the medium scale analyses poorly predict the ultimate capacity of the structural wall. As reported in table 4.5, the first load peak after the drift-off from the experimental result is only about 63% of the experimental load capacity. After this point, the analyses behave very differently, and while the rotating crack model never reaches a higher load, the fixed crack model predicts an ultimate load at 72% of the experimental capacity at a displacement of 23 mm. However, the prediction of the wall behavior before the initial load peak is very good in both crack models. Both the load and deflection at initiation of flexural cracking is in good agreement with the reported experimental results. And, as described by Lefas et al., the crack pattern spreads out both vertically and horizontally from the bottom of the tensile zone, gradually inclining towards the bottom left corner of the wall. The shear forces in the wall also comply with the shear behavior described by Lefas et al., i.e. the shear resistance contribution from the fully cracked zone of the wall is small, and the shear forces are transferred to the wall base through the compressive zone. It is evident from the analyses that the critical area that governs the failure of the wall is the bottom left corner. The failure mode is the same as seen in the experimental results: splitting of the compressive zone. This failure is seen before yielding of the reinforcement occurs, the opposite of the behavior found in the experiment where the reinforcement shoved significant plastic deformations before the capacity of the wall was reached. These results indicate that the poorly predicted capacity of the wall is caused by the inability of the finite element model to fully predict the stress state in the compressive zone and thus the true capacity of this zone is not utilized.

A comment should be made on why the behavior of the two crack models is similar until the shift of the compressive zone occurs. The initiation of the crack pattern is handled in the same way by both models: the strains are evaluated in the principal

strain directions. The two models should predict the same behavior unless a significant rotation of the stress field takes place after initiated cracking, or if the initial crack in an integration point is not representative for the crack pattern in its corresponding area. In the analyses presented, no significant rotation of the stress field is seen until after the shift of the compressive zone, and the initial crack directions are more or less correct. Thus, the models predict the same structural response until this stage. After the shift of the compressive zone the stress field rotates towards the front of the new compressive zone, and the differences in the two crack models become apparent. In the rotating crack model, the rotation is allowed to occur and the capacity is quickly reduced. In the fixed crack model on the other hand, the crack pattern is locked in the initial configuration and the predicted response is stiffer than predicted by the rotating crack model, causing the wall to regain capacity.

The regained capacity after the initial load peak will not be given much consideration in the following discussion. The aim of this thesis is to investigate how NLFEA can be utilized in a design process. In a design situation the drop in load capacity observed after the initial peak would most likely be considered structural failure, and the load at the initial load peak would be regarded as the ultimate load. Notice also how both the compressive and the shear stress capacity of the initial compressive zone is negligible after the initial load peak. Thus, the wall after the load peak can almost be considered a narrower version of the wall before the load peak. The fact that an even higher capacity is found after the load peak for the fixed crack model raises suspicion. However, based on the argument stated above, this part of the wall deflection will not be discussed in detail.

5.2 Large Scale Analyses

The predicted ultimate load of the large scale analyses is better than for the medium scale analyses. The ultimate load of both the fixed and rotating crack models is 84% of the experimental capacity of the wall. Despite the large element size, the analyses are able to predict the initiation and propagation of the crack pattern rather well. As seen in the medium scale analyses, the distribution of shear forces in both large scale analyses also comply with the experimental result. Shear stresses are carried by a shear band stretching from the top edge of the wall to the compressive zone in the bottom left corner. Notice that the element size used in the large scale analyses cause shear stresses to appear on the left edge of the wall, i.e. no pure compressive column is seen. The analyses predict yielding of the vertical reinforcement at an external load of 78

and 79 kN for the fixed and rotating crack models, respectively. This load compares well with the reported external load of 80 kN from the experiment. What is more interesting is that yielding is predicted before the failure of the compressive zone, just as reported from the experiment. The analyses fail to model the triaxial stress state in the initial compressive zone, resulting in a premature failure. However, as for the medium scale analyses both large scale analyses fail due to splitting of the compressive zone, in agreement with the experimentally reported failure mode.

5.3 Volumetric Expansion Effect

The inability of all analyses to model the triaxial stress state in the compressive zone is believed to be the most important factor of the poor prediction of the ultimate load capacity. Lefas et al. discuss how the volume dilatation effect described in section 2.1.3 is the main cause of the triaxial conditions observed in the compressive zone in the experiment [14]. When the expansion of the highly stressed concrete in this region is restrained, a triaxial stress state is created which significantly increases the compressive strength of the concrete. The restraint is caused by adjacent concrete regions or, as pointed out by Lefas et al., mainly by the confining stirrup reinforcement in the wall columns.

When the results of the medium and large scale analyses are examined closer an interesting observation is done. It is found that the mean stress of the most critical stirrup reinforcement bar in the compressive zone is increased from 60 to 320 MPa between load steps 10 and 11 in the medium scale analyses, and from about -10 to 233 MPa between load steps 15 and 16 in the large scale analyses. These load steps correspond to the last step before splitting and the first step after splitting, respectively. Both the fixed and rotating crack model yield this result and similar behavior was found for the main horizontal reinforcement in this region. The stress increase in the reinforcement occurs after the concrete in this region has passed its most stressed state in load step 8 in the medium scale analyses, and in load step 15 in the large scale analyses. This indicates that significant lateral expansion of the elements in the compressive zone does not occur until after failure of this region. The concrete stresses in both the global x- and y-directions for the medium scale fixed crack analysis are plotted in figure 5.1 for integration points 1 and 2 (cf. figure 4.15), located at the front of the initial and the shifted compressive zone, respectively. The figure clearly shows how a significant biaxial stress state causes an increase of the concrete strength in integration point 2. It is also evident that the confining stresses are small in integration point 1 before the shift.

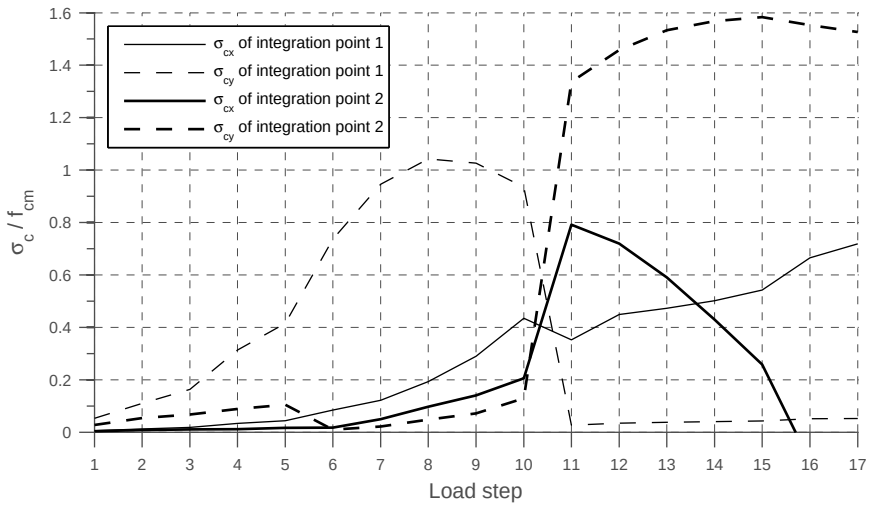

Figure 5.1: *Biaxial stress states in the fixed crack model*

Judging by the results presented, it is believed that a finite element model that is capable of producing a proper biaxial stress state in the initial compressive zone probably will predict a more accurate capacity of the structural wall. It seems that an implementation of the volumetric expansion effect described in section 2.1.3 could help develop the full biaxial stress state in the compressive zone. Selby and Vecchio state that the lateral expansion effects of concrete can not be neglected in problems where triaxial stress conditions are central [25]. In figure 5.2(a) the volumetric strain for the fixed crack model is presented for both the medium and large scale analyses. The location of the integration points M_A, M_B and M_C, representing values from the medium scale analysis, is illustrated in figure 5.2(b). The integration point L from the large scale analysis, is the point where splitting is observed in figure 4.28(e). The point of minimum volume for each of the integration points in figure 5.2 is reached in the last step before splitting is observed (cf. figure 4.17(d), 4.17(e) and 4.28(d)), i.e. after the compression strength of the concrete is reached. As described in section 2.1.3, the point of minimum volume should have occured at 80-95% of the compressive strength. When a volumetric expansion is not present at an earlier stage, the capability of the stirrup reinforcement to create a biaxial stress state is not utilized properly. If a proper implementation of the volume dilatation effect was done, volumetric expansion would have occurred in an earlier load step and probably allowed for a more correct biaxial stress state and consequently an increased capacity of the structural wall. It should be

noted that the the course of the volumetric strain until the point of minimum volume is not non-linear as can be perceived from figure 5.2(a). If the strain was plotted against the principal stress it would be linear due to the constant Poisson's ratio used in the analysis.

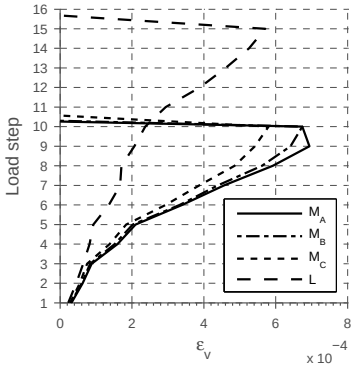

(a) *Volumetric strain*

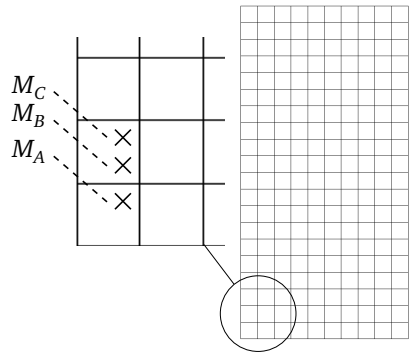

(b) *Medium scale integration points*

Figure 5.2: *Predicted volumetric strain from the fixed crack model*

Finite element analysis of the structural wall experiments reported by Lefas et al. has previously been conducted by other researchers. Selby and Vecchio reports the result of such an analysis of structural wall SW16 [25]. The height-to-width ratio of this structural wall is different from the wall analyzed in this thesis but the deformational response is similar, and the failure of the wall is governed by the strength of the concrete in the compressive zone. The wall was modeled in 3D as seen in figure 5.3(a) and a rotating crack model with similar material models to the ones presented in section 2.2 was used. What makes this analysis interesting is the inclusion of the volumetric expansion effect, achieved by increasing the Poisson's ratio when the stress approaches the ultimate strength of the concrete. The load-deflection curves of the analyses presented in figure 5.3(b) clearly show how the prediction of the ultimate load is in good agreement with the test results, if a lateral confinement model for the concrete is specified. If no lateral confinement model is specified, premature failure of the wall is observed. The writers report that the concrete stress at peak load is $1.52f_{cm}$. The increase in strength is attributed to the stirrup reinforcement and the concrete area of the bottom beam surrounding the compressive zone of the wall. Both help create a triaxial stress state by retaining the expanding concrete. At the peak load, the stirrup reinforcement was approaching yield, thus a substantial contribution to the triaxial stress state from

this reinforcement is present. The results from Selby and Vecchio clearly show the importance of the volumetric expansion effect when triaxial stress states govern the load capacity of a reinforced concrete member.

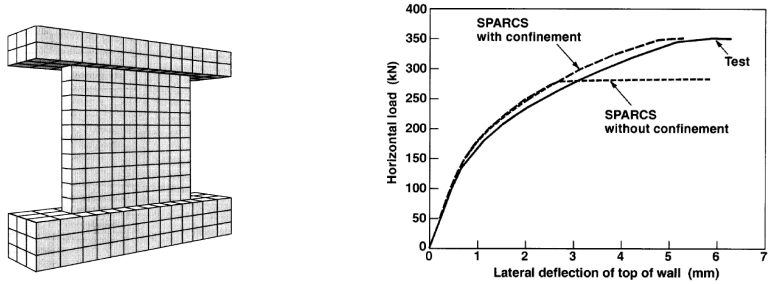

(a) *Finite element model* **(b)** *Analysis result*

Figure 5.3: *SW16 analyzed by Selby and Vecchio [25]*

5.4 Effect of Element Size

The use of large elements can cause inaccurate results in the analyses since large elements means fewer integration points for describing the structural behavior. In order to determine if the analysis result is sufficiently accurate, and if the result is usable in a design process, the effects of the element size is investigated.

5.4.1 Effects Observed in the Case Study at Hand

The step from medium scale elements to large scale elements has some implications on the behavior of the structural wall tested, and some immediate observations can be done on basis of the presented results. First of all it is evident that the predicted capacity of the wall is increased when modeled with larger elements. Secondly, the crack pattern in the large scale analyses is comparable to the crack pattern seen in the medium scale analyses and the failure mode is correct. Thirdly, yielding of the reinforcement initiates before the load peak in the large scale analysis, while the opposite is observed at medium scale. To help expose the general differences between the two element sizes, the changes in the wall stiffness during each analysis can be compared. The prediction of the wall stiffness is an important aspect of the analyses and can reveal valuable information about the deformational response. The secant stiffness for the medium and large scale fixed crack analyses, and the experimentally reported results are plotted against the external load in figure 5.4. Note that the curves are cut off at the peak load. The plot shows how the experimental stiffness is rapidly decreased

in the start of the wall deformation and how it stabilizes at about 40 kN. At 80 kN, an inflection point is reached and the stiffness is decreasing more rapidly toward the ultimate load. The inflection point corresponds to the observed yielding of the vertical reinforcement in the experiment. Except from the too stiff prediction of the secant stiffness until an external load of 40 kN, the plot shows a good correlation between the experimental and the analysis stiffness. Note also that the secant stiffness of the large scale analysis inflects at 80 kN, when yielding is initiated, thus the change in stiffness associated with this point in the experiment is captured by the analysis. The predicted secant stiffness indicates that both analyses approximate the behavior of the wall quite well, despite the premature failures. The main difference observed between the medium and large scale analyses in the plot, is the stiffer behavior exhibited by the large scale analysis during the start of the deformational response. This difference is probably caused by the development of the crack pattern on the tensile edge of the wall. As reported in table 4.5, the medium and large scale analyses predict initiation of flexural cracking at 13 kN in load step 2 and 17 kN in load step 3, respectively. The two load steps without cracking in the large scale analysis is evident by the initial horizontal course of the secant stiffness in figure 5.4. Before cracking is initiated, and at low levels of compressive stress, the response of the wall is linear and thus the secant stiffness remains unchanged.

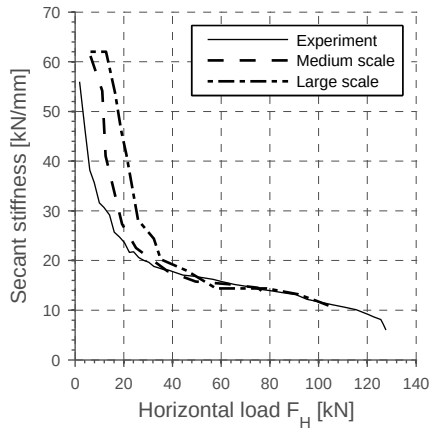

Figure 5.4: *Secant stiffness from the fixed crack model*

The softer behavior seen in the first phase of the secant stiffness plot for the medium scale analysis, as compared to the large scale analysis, is believed to be caused by localization of the crack pattern. When cracking is initiated in an integration point,

unloading in the surrounding integration points is observed. An increase in the external load on the structural wall causes the strains in the existing cracks to increase along the tension softening path, and the strains in the neighboring areas to decrease due to the elastic unloading. The result is a decrease in stresses in both areas and thus a softer behavior of the structure. In the large scale analyses, the fracture process is non-localized and each integration point represents a larger area, thus the localization and unloading observed in the medium scale analyses is not present and the wall response is stiffer. The difference between the localized and non-localized crack patterns is evident in figure 5.5, showing the results of the medium and large scale analyses at an external load of about 20 kN. When the crack pattern is progressed further, the differences in the medium and large scale analyses are not so prominent and the initial difference in the secant stiffness predicted by the two analyses, as seen in figure 5.4, is decreased. As seen in figure 5.6, the predicted crack patterns in the two analyses are very similar at an external load of about 40 kN. Note that the mesh of the large scale analyses is outlined in the medium scale plots in figures 5.5 and 5.6 to allow for effective comparison of the two analyses.

In both the medium and large scale analyses, splitting is not observed in the bottom most integration points, probably due to the restraining of the nodes along the wall base. The absence of splitting in these points is not believed to have much of an influence on the medium scale analyses where the elements are rather small, and thus the bottom elements alone do not govern the behavior of the compressive zone. However, in the large scale analyses, the restrained nodes could cause a higher capacity in the compressive zone. Here, the critical area of the compressive zone is covered by only one element and the restraining of the nodes in that element therefore affects a rather large area of the structural wall. Also, the width of the compressive zone found in the medium scale analyses (cf. figure 4.11 and 4.11) is only about $1/3$ of the side length of the elements used in the large scale analyses. Thus, the area covered by the element in the compressive zone in the large scale analyses experiences both compressive crushing and tensile cracking, a large diversity in the material behavior represented by only four integration points. The most extreme compressive stresses occurring in this area is not picked up by the integration points in the element and the failure of the compressive zone is delayed. It is believed that this is the main contribution to the higher capacity predicted by the large scale analyses. However, despite this behavior, the large scale analyses provide a conservative prediction of the load carrying capacity of the structural wall, and the response is well predicted until failure.

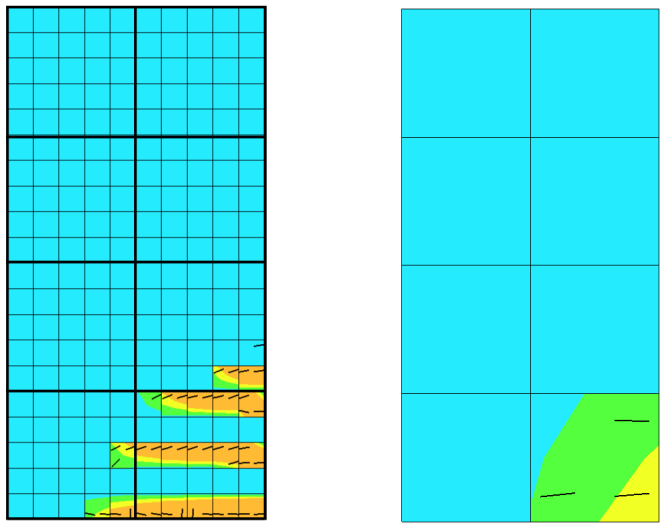

(a) *Medium scale crack pattern at 20 kN*

(b) *Large scale crack pattern at 19 kN*

Figure 5.5: *Localized **(a)** and non-localized **(b)** crack patterns*

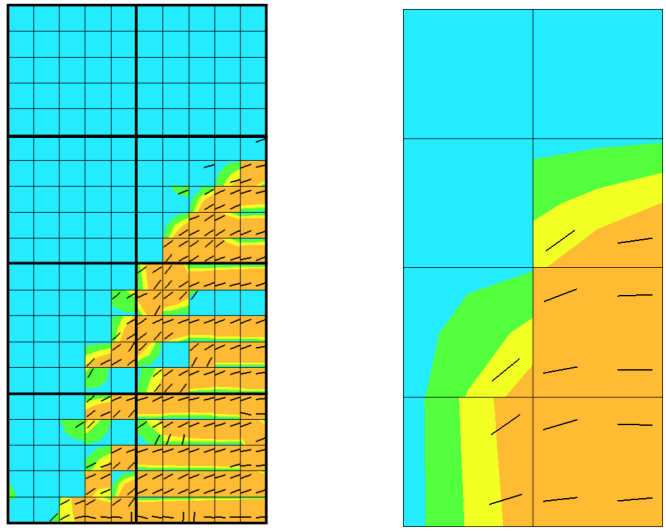

(a) *Medium scale crack pattern at 38 kN*

(b) *Large scale crack pattern at 36 kN*

Figure 5.6: *Progressed crack patterns*

5.4.2 The use of Large Elements in a Design Process

When generalizing the effects of the element size, while keeping in mind the suggested utilization of NLFEA in a design process, three main aspects are important. As discussed in chapter 3, NLFEA should provide the analyst with information about the correct distribution of forces in the structure, the correct load capacity and the cause and progression of failure. The analyses conducted here have shown that the use of large scale elements will accurately predict the stiffness of the structural wall, at least for high load levels. Accurate prediction of the stiffness means accurate prediction of the deformations, and this is essential for the utilization of NLFEA in a design process. If the structural wall discussed here was part of a larger structure, the predicted stiffness would have a large influence on the load distribution in the structure. If an accurate distribution of forces in the structure is sought, the stiffness of each structural part must be accurately predicted. The results of the analyses conducted here show that a well predicted load distribution can be expected when large scale elements are used for modeling of structural members.

When it comes to finding the ultimate load carrying capacity of the structure the analyses have shown that the material models used here would probably not yield a satisfactory degree of accuracy without including the volumetric expansion of the concrete. This is true for both the medium and large scale analyses, and the effect of the element size on the accuracy of the predicted load capacity can therefore not be studied thoroughly. It might well be that the large scale analyses would predict a non-conservative ultimate load if the material models in general performed more accurate, due to the generally stiff nature of structures modeled with large elements.

The last sought after result is the cause and progression of failure in the structure. The analyses have shown that the large scale model predicts the failure mode correctly, despite the premature failure. After the initial peak load, the load capacity of the wall is greatly reduced and the deflection similarly increased. If part of a larger structure, the load carried by the structural wall would have to be redistributed to other parts of the structure, and thus the progression of failure in the structure could be followed on a global level.

It should be pointed out that the results found here are based on the analyses of the structural wall alone. Analyses of a wide range of structural components must be conducted to verify that the results obtained here are valid in general, before NLFEA with large scale elements can be confidently utilized for large structures.

6 Concluding Remarks

The results presented suffer from the lack of a well predicted ultimate load carrying capacity of the structural wall, both in the medium and large scale analyses. The premature failure seen in all analyses complicates the finding of effects caused by the element size. If better results were obtained in the medium scale analyses, the differences that occur in the transition to large scale elements would probably be more noticeable and easier to single out. However, despite these difficulties, some concluding remarks can still be done:

1. It is clearly evident that the predicted ultimate load carrying capacity of the structural wall is highly affected by the triaxial stress state in the compressive zone, and that the premature failure observed in all analyses are caused by the inability of the finite element model to reproduce such a stress state. Based on the discussion of the results presented here, and the results obtained by other researchers, it is concluded that the volumetric expansion effect of the concrete must be respected in order to accurately predict the ultimate load by use of NLFEA.

2. In the medium scale analyses, a significant difference between the fixed and rotating crack models is found in the wall response after the failure of the initial compressive zone. The increased capacity observed in the fixed crack model is questioned. However, the subject has not been further investigated, due to the fact that the response after the initial peak load is of little importance in a design situation as the one presented here.

3. No significant difference is seen between the fixed and the rotating crack model before the initial peak load. The small difference is attributed to the fact that the first initiation of cracks are representative for the fully developed crack pattern, and thus no significant rotation of the stress field is observed in the analyses when the crack pattern progresses to its final state at the peak load.

4. Based on remarks 2 and 3, use of the rotating crack model is advised to allow for a conservative analysis result. However, if a rotation of the stress field is expected, the rotating crack model may yield a result that is too conservative and use of the fixed crack model should be considered.

5. The predicted wall behavior is stiffer in the large than in the medium scale analyses during the initiation of cracks. It is believed that the localization of the

crack pattern in the medium scale analyses causes a softer behavior of the wall during the crack initiation. On the contrary, the non-localized crack pattern in the large scale analyses yields a stiffer result. When the crack pattern is further developed, the representation of the pattern is very similar in the two models, and the difference in the predicted stiffness is negligible.

6. The higher load carrying capacity obtained by the large scale analyses is mainly believed to be caused by the inability of the large elements to pick up the most extreme compressive stresses in the compressive zone. Thus, the failure of the compressive zone is delayed and a higher load capacity is found.

7. The large elements used in the large scale analyses are able to predict the stiffness of the structural wall accurately, and thus the deformational response of the wall is equally well predicted. It is believed that the use of such elements in the analysis of a large structure would allow for an accurate global load distribution to be found.

8. The failure mode of the structural wall is predicted correctly by the large elements, and the crack pattern is accurately reproduced. If part of a larger structure, the accurate prediction of failure predicted by the large elements would allow for finding the cause and progression of failure in the structure. However, is should be reminded that structural members other than structural walls, have not been accounted for in this thesis.

9. The large scale analyses fail to predict the correct ultimate load carrying capacity of the structural wall analyzed, and a correct prediction of the load capacity of a larger structure should therefore not be expected. However, as pointed out in remark 1, the poor prediction of the ultimate load is attributed to the missing volumetric expansion of the concrete. Thus, the effect of the large scale elements on the load carrying capacity has not been singled out. If a proper implementation of the volumetric expansion effect was done, it could very well be that the large scale elements would yield a non-conservative prediction of the ultimate load, due to the generally stiff nature of finite element models with large elements.

Apart from the poorly predicted load carrying capacity, the use of large scale elements in NLFEA of large structures has proven to be promising. However, a lot of work still remains before analyses can be conducted with confidence. Suggestions for further work within this subject is given in the next chapter.

7 Suggestions for Further Work

1. Work needs to be done to find a suitable material model that respects the volumetric expansion of concrete. Several such material models exist, but none of them are implemented in DIANA. Whatever finite element program is to be used for conducting the NLFEAs, the volumteric expansion effect must be implemented. The model presented by Selby and Vecchio [25] can be used. Material models proposed by Kotsovos et al. [26], that respect the volumetric expansion on a more fundamental level, can also be used.

2. The difference in the fixed and rotating crack models should be investigated further, such that analyses of structures that experience a rotation of the stress field can be conducted with confidence.

3. Analyses must be conducted on a wide range of structural components to verify the results obtained here in a more general sense. Components that display a different crack pattern and a different failure mode, than seen in the structural wall investigated here, should be investigated.

4. Only one element size was used for the large scale analyses in this thesis. The element size was chosen as the maximum justifiable size based on the results of preliminary linear analyses of the structural wall. If analyses are conducted with several element sizes, the transition from medium to large scale can be investigated in more detail.

5. In the design of a large structure, 3D analysis is most likely to be used. The analyses presented here were only conducted using 2D models. The 3D behavior of the material models used here, should be investigated before they are utilized in a design process.

References

[1] F. J. Vecchio. Non-linear finite element analysis of reinforced concrete: at the crossroads? *Structural Concrete*, 2(4):201–212, 2001.

[2] R. G. Selby and F. J. Vecchio. *Three-dimensional constitutive relations for reinforced concrete*. University of Toronto, Department of Civil Engineering, 1993.

[3] Kolbein Bell. *An engineering approach to FINITE ELEMENT ANALYSIS of linear structural mechanics problems*. Akademika Publishing, 2013.

[4] The International Federation for Structural Concrete (fib). Bulletin 45: Practitioners' guide to finite element modelling of reinforced concrete structures, 2008.

[5] H Kupfer, H. K. Hilsdorf, and H. Rusch. Behavior of concrete under biaxial stresses. *ACI Journal*, 66:656–666, 1969.

[6] M. D. Kotsovos. Effect of testing techniques on the post-ultimate behaviour of concrete in compression. *Matériaux et Construction*, 16(91):3–12, 1983.

[7] F. J. Vecchio and M. P. Collins. Compression response of cracked reinforced concrete. *Journal of Structural Engineering*, 119(12):3590–3610, 1993.

[8] R. H. Evans and M. S. Marathe. Microcracking and stress-strain curves for concrete in tension. *Matériaux et Construction*, 1(1):61–64, 1968.

[9] Task Group 8.7. Code-type models for concrete behavior. In *Background of MC2010*, number 70 in bulletin. fib, 2013.

[10] Rijkswaterstaat Centre for Infrastructure. Guidelines for nonlinear finite element analysis of concrete structures, May 2012.

[11] B. H. Oh and Z. P. Bazant. Crack band theory for fracture of concrete. *Matériaux et Constructions*, 16(93):155–177, 1983.

[12] F. J. Vecchio and M. P. Collins. The modified compression-field theory for reinforced concrete elements subjected to shear. *ACI Journal*, 22:219–231, 1986.

[13] J. G. Rots and J. Blaauwendraad. Crack models for concrete, discrete or smeared? fixed, multi-directional or rotating? *HERON*, 34(1):1–59, 1989.

[14] I. D. Lefas, M. D. Kotsovos, and N. N. Ambraseys. Behavior of reinforced concrete structural walls: strength, deformation characteristics, and failure mechanism. *ACI Structural Journal*, 87(1):23–31, 1990.

[15] F. González-Vidosa, M. D. Kotsovos, and M. N. Pavlovic. On the numerical instability of the smeared-crack approach in the non-linear modelling of concrete structures. *Communications in applied numerical methods*, 4(6):799–806, 1988.

[16] Peter Hendrikus Feenstra. *Computational aspects of biaxial stress in plain and reinforced concrete*. PhD thesis, Delft University of Technology, 1993.

[17] TNO DIANA BV. *DIANA User's manual*, 9.4.4 edition, 2012.

[18] B. Belletti, C. Damoni, J. A. den Uijl, M. A. N. Hendriks, and J. C. Walraven. Shear resistance evaluation of prestressed concrete bridge beams: fib model code guidelines for level iv approximations. *Structural Concrete*, 14(3):242–249, 2013.

[19] M. D. Kotsovos, M. N. Pavlovic, and D. M. Cotsovos. Characteristic features of concrete behaviour - implications for the development of an engineering finite-element tool. *Computers and Concrete*, 5(3):243–260, 2008.

[20] The International Federation for Structural Concrete (fib). Model code 2010 - final draft, 2012.

[21] D. E. Brekke, E. Aldstedt, and H. Grosch. Design of offshore concrete structure based on postprocessing of results from finite element analysis (fea): Methods, limitations and accuracy. In *The Proceedings of the 1994 International Offshore and Polar Engineering Conference*, volume 4, pages 318–328. International Society of Offshore and Polar Engineers, 1994.

[22] R. Lackner and H. A Mang. Scale transition in steel-concrete interaction. i: Model. *Journal of engineering mechanics*, 129(4):393–402, 2003.

[23] M. D. Kotsovos, M. N. Pavlovic, and S. Arnaout. Nonlinear finite element analysis of concrete structures - a model based on fundamental material properties. In *Proceedings of the NUMETA '85 Conference*, 1985.

[24] J. A. Øverli. *TKT422 Concrete Structures 3 Compendium*. Department of Structural Engineering NTNU, 2013.

[25] R. G. Selby and F. Vecchio. A constitutive model for analysis of reinforced concrete solids. *Canadian Journal of Civil Engineering*, 24(3):460–470, 1997.

[26] M. D. Kotsovos and J. B. Newman. A mathematical description of the deformational behaviour of concrete under complex loading. *Magazine of Concrete Research*, 31(107):77–90, 1979.

[27] R. D. Cook et al. *Concepts and applications of finite element analysis*. John Wiley & Sons, 2007.

Appendices

A Model Generations

This appendix contains descriptions of the different finite element models created, from the first to the last generation. For each model, the geometry, boundary conditions and load application is specified, and problems encountered when using the model are discussed.

A.1 First Generation Model

In the initial modeling of the structural wall, all geometric data reported from Lefas et al. [14] was taken into account. Both the top and bottom beams, and all reinforcement bars were included in the finite element model. It was reported from the experiment that the bottom beam was clamped to the laboratory floor on either side of the wall itself. Thus, certain nodes on the top side of the bottom beam, roughly corresponding to the clamped area in the experiment, were fixed in both the x- and y-directions. All nodes along the bottom edge of the bottom beam were also fixed in both of the global directions. Loading was applied as evenly distributed along the right edge of the top beam. Specified boundary conditions and applied loading is illustrated in figure A.1(a).

When investigating the results of the NLFEA, extensive cracking, illustrated in figure A.1(b), was discovered in the bottom beam. It was suspected that these cracks caused a negative influence on the behavior of the structural wall. Measures were done to eliminate this influence and the second generation model was made. The details of the second generation model are described in appendix A.2.

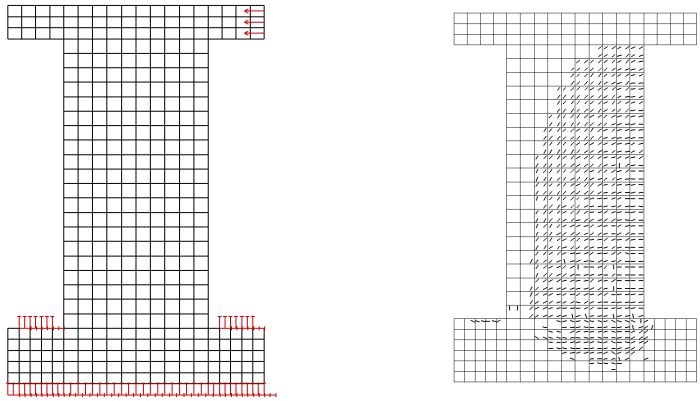

(a) *Element mesh* **(b)** *Crack pattern*

Figure A.1: *First generation model*

A.2 Second Generation Model

The second generation model was created due to the extensive cracking observed in the bottom beam of the first generation model (cf. figure A.1(b)). It was decided to remove the bottom beam completely and fix all the nodes along the bottom edge of the wall in the x- and y-directions. The fixed wall base was justified by measurements performed during the experiment, confirming a fixed wall base [14]. As in the first generation model, loading was applied as evenly distributed along the right edge of the top beam. Specified boundary conditions and applied loading is illustrated in figure A.2(a).

Problems with the second generation model were discovered when implementing a bond slip relation. It was found that the bond slip was highly localized in the tensile zone along the wall base, as shown in figure A.2(b). This localization caused the wall to fail for extremely low values of externally applied loading. The behavior was thus deemed unnatural and a last generation model was created to avoid the localized bond slip. The details of the last generation model are described in appendix A.3.

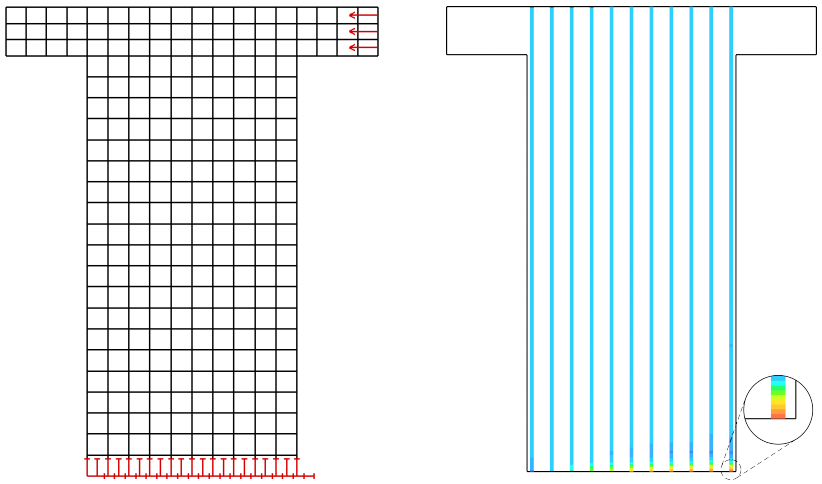

(a) *Element mesh* **(b)** *Bond slip localization*

Figure A.2: *Second generation model*

A.3 Last Generation Model

The last generation model was created to avoid the localized bond slip observed in the NLFEA of the second generation model (cf. figure A.2(b)). It was suspected that the localization was caused by the fixed ends of the reinforcement bars along the wall base. An extended area of the concrete below the wall base was therefore modeled to allow for proper anchoring of the reinforcement bars, and thus a gradually increasing transfer of tractions between the concrete and reinforcement. The height of this extended area was set equal to the height of the bottom beam as specified in the experiment by Lefas et al. (cf. figure 4.1). The vertical reinforcement bars were extended below the wall base and bent towards the outer edges of the wall (cf. figure 4.5(a)). All nodes along the initial wall base were fixed in the x- and y-directions. In this way, the deformations of the wall was not affected by the extended concrete area below the wall base. As in the models of the previous generations, the loading was applied as evenly distributed along the right edge of the top beam. Specified boundary conditions and applied loading is illustrated in figure A.3(a).

The NLFEA result revealed a proper localization pattern of the bond slip, were the effect of the bond slip was spread out vertically in the tensile zone of the wall. The localized bond slip pattern is illustrated in figure A.3(b).

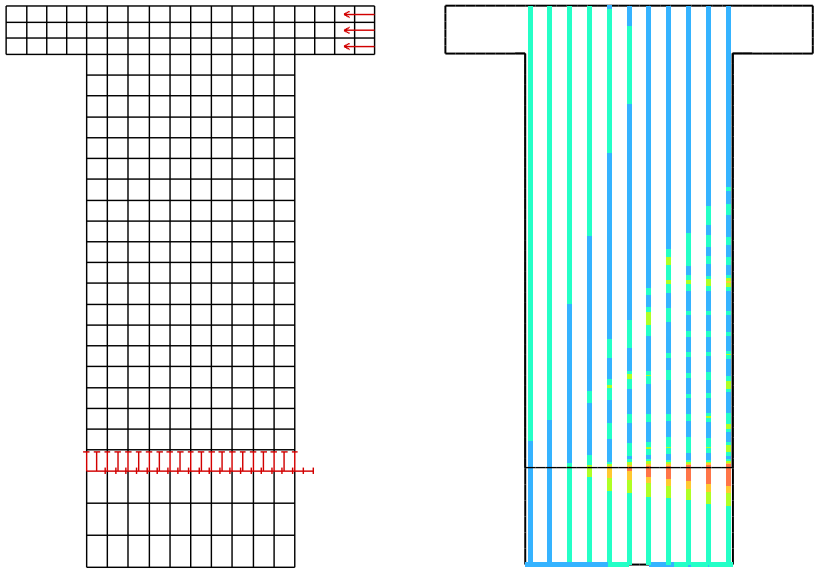

(a) *Element mesh* **(b)** *Bond slip localization*

Figure A.3: *Last generation model*

B Problems Encountered in DIANA

This appendix contains documentation of the problems met when using the DIANA finite element program. The background and solution for each problem is described. This appendix will be of use for future analysts facing similar problems when using the program.

B.1 Obtaining the Correct Reinforcement Stresses

The implementation of bond slip in DIANA utilizes the CQ22IF interface element (cf. section 4.3.3) for handling the relative slip and the transfer of traction stresses between the concrete and reinforcement elements. When the element is present, it is no longer possible to obtain the stresses from the integration points of the reinforcement elements, and consequently these stresses must be sampled in the nodes. The nodes, integration points, displacement field and stress field of the reinforcement element are illustrated in figure B.1. According to finite element theory, stresses are most accurate when sampled in the reduced Gaussian integration points [27]. In order to obtain the reinforcement stresses with the highest accuracy, an interpolation of the stresses was done. The stresses were first sampled at all the 3 nodes in each element. Secondly, a control of these stresses was made, to check that an expected linear variation (due to the differentiated interpolation functions used for calculation of stresses and strains) between the 3 nodes was present. At last, the nodal values for the stresses were interpolated to find the stress values at the position of the reduced Gaussian integration points. With this approach it was possible to obtain accurate reinforcement stresses to which post-processing could be applied. The approach is cumbersome, and direct export of stress values from the integration points, when using interface elements, should be implemented natively in DIANA.

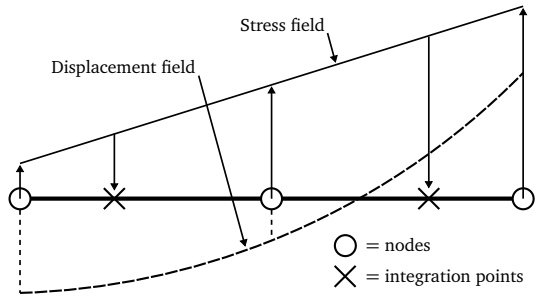

Figure B.1: *Interpolation of stresses*

B.2 Obtaining Slip and Traction Values

To monitor that DIANA was indeed following the bond slip curve from *fib* Model Code 2010 (cf. section 2.2.7), it was necessary to export the traction and slip values from each interface element. However, obtaining these values proved more challenging than expected. DIANA does not allow the export of traction and slip values from the integration points of the CQ22IF interface element, used for implementation of bond slip. Only values from the nodes are available. At first, the interpolation approach used for obtaining the reinforcement stresses (cf. section B.1) was applied to interpolate the values from the nodes back to the integration points. However, it turned out that the CQ22IF interface element does not utilize a Gaussian integration scheme. The DIANA manual does not specify the integration scheme, the position, or thr number of integration points used in the element. At last, the values were obtained by directly opening the database created by the analyses in DIANA. The database can be read through the DIANA Command Box as shown in figure B.2. The figure shows the commands needed to access integration point 1 in element 9 of reinforcement bar 69. Values are printed by calling the commands ”p TRA” and ”p U” which prints the traction and slip values stored to the database at the end of the last load step, respectively. The values in the database are overwritten at the end of each load step, and consequently only values from the last load step is available. However, the commands ”p TRA.s” and ”p U.s” will print the values from the start of the last load step, which are identical to the values at the end of the preceeding load step. The wanted values are the first reported under each command in figure B.2. Thus the traction and slip values at the end of the last load step for the integration point in the figure are 9.43 MPa and 0.3097 mm, respectively.

Values obtained from a few chosen integration points proved that DIANA was following the material curve specified. It was assumed, without further monitoring, that this was the case for all other integration points in the finite element model. The approach is not satisfying and does not allow the analyst to check the traction and slip values in all integration points without repeating the process illustrated in figure B.2. It is evident that almost any finite element model of a concrete structure will contain enough integration points to safely regard this approach unusable. Thus, proper export of the traction and slip values directly from the integration points should be implemented in DIANA.

```
                        +------------------------+
                        | Welcome to DIANA       |
                        | Release 9.4.4          |
                        +------------------------+

C:\User\username> cd C:\database\directory
C:\database\directory> START lq .diana/ff
lq> cd /REINFO(69)/ELEMEN(9)/INTPT(1)
lq> p TRA
9.430e+000 -1.210e-006
lq> p U
3.097e-001 -2.521e-010
lq> p TRA.s
9.130e+000 -1.209e-006
lq> p U.s
2.855e-001 -2.519e-010
```

Figure B.2: *Command code for obtaining slip and traction values*

B.3 Trilinear Reinforcement Material Curve Convergence Problems

As described in section 2.2.7, a trilinear stress-strain relationship was used to avoid numerical trouble when the stress exceeds the yield strength in a load step. The material curve was successfully used in the medium scale analyses, but problems were encountered in the large scale analyses. As illustrated in figure B.3, the stress values reported immediately after yielding are far from the correct values, both in compression and tension. Convergence immediately after yielding is not found. However, global equilibrium was achieved and DIANA reported a converged load step. Thus, the severe mis-calculation of stresses on the material level was never reported to the end-user. To confirm that the stress values were indeed the values found in the integration points, the values were extracted directly from the analysis database, using the same approach as is illustrated in figure B.2, in addition to the usual approach of exporting them from FEMVIEW in DIANA. It is believed that the differences in the tangential stiffness in the material curve before and after yielding prevents the program from finding convergence. It is also believed that the maximum number of iterations was used, and that this forced the program to continue to the next load step although convergence was not found. However, this was not confirmed. A solution of the convergence problem was found by specifying the original bilinear stress-strain curve. As is evident in figure B.4, all load steps are converged on the material level when using the bilinear curve.

It is worrying that DIANA will continue to the next load step when the stress in the material is so far from the correct stress, without notifying the end user. It is also peculiar that the program is unable to find convergence when met with such a soft nonlinearity. It could be an indication that the iterative scheme used for finding the material stresses is perhaps not optimal.

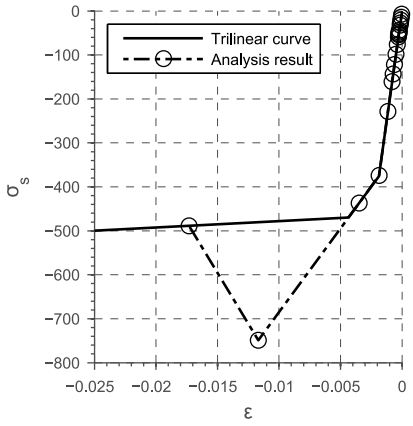

(a) *Reinforcement bar in compression*

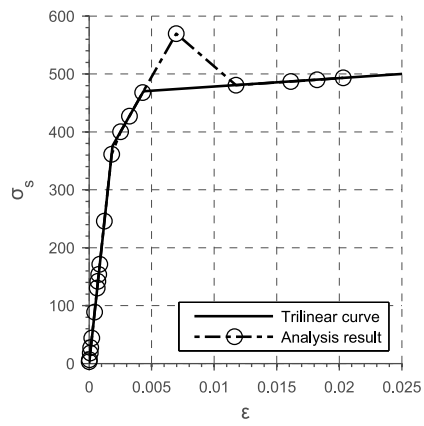

(b) *Reinforcement bar in tension*

Figure B.3: *Trilinear material curve*

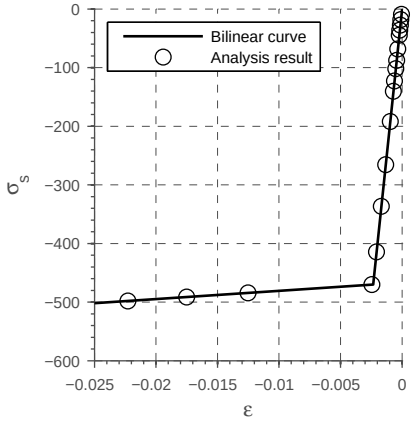

(a) *Reinforcement bar in compression*

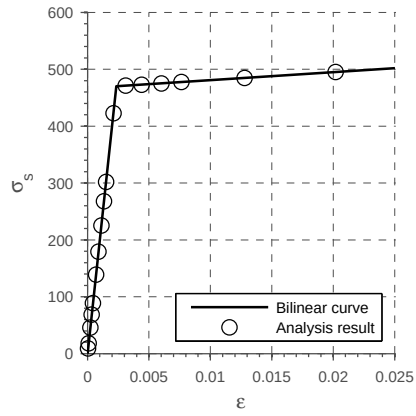

(b) *Reinforcement bar in tension*

Figure B.4: *Bilinear material curve*